# Design and Characteristics of a Low Temperature Atomic Force Microscope

Mark A. Roseman
Centre for the Physics of Materials
Department of Physics
McGill University
Montréal, Québec
Canada

A Thesis submitted to the
Faculty of Graduate Studies and Research
in partial fulfillment of the requirements for the degree of
Master of Science

# Contents

# List of Figures

# List of Tables

# Abstract

A low temperature atomic force microscope has been designed and built. The instrument will operate at liquid helium temperatures, and will be used to investigate a number of phenomena observable only at low temperatures, including flux pinning mechanisms in superconductors, as well as domain structure dynamics in microfabricated ferromagnetic particles.

This thesis provides a general review of force microscopy, including a summary of the forces to which the instrument is sensitive, as well as the most common modes of operation of the force microscope. An overview of our newly constructed low temperature microscope is then presented, examining each of the components in detail. In addition, the problems of mechanical vibration isolation, thermal properties of materials at low temperatures, as well as remote in-situ manipulation are discussed.

# Résumé

Un microscope à force atomique à basse température a été conçu et bâti. L'instrument fonctionnera à la température de l'hélium liquide, et sera utilisé pour étudier plusieurs phénomènes observables seulement à basse température, incluant les mécanismes d'ancrage de flux dans des supraconducteurs ainsi que la dynamique des structures de domaines dans des particules ferromagnétiques mirofabriquées.

Cette thèse donne une revue générale de la microscopie de force, incluant un sommaire des forces auxquelles l'instrument est sensible, aussi bien que les modes d'opérations les plus courant du microscope de force. Une vue d'ensemble du microscope à basse température est alors présentée, examinant tous les composants en détails. De plus, les problèmes d'isolations des vibrations mécaniques, des propriétés thermiques des matériaux à basses températures ainsi que de la manipulation in situ à distance sont discutés.

# Acknowledgments

Firstly, I would like to thank my supervisor, Dr. Peter Grütter, for entrusting me with this project. His patient guidance over the past two years have made this a very enjoyable experience. I look forward to the next few years. I would also like to thank Dr. Brett Ellman for introducing me to the world of low temperature physics. His advice and help have been invaluable.

It wouldn't have been as much fun without all my friends in the department. In particular, thanks to Matt Borthwick, Dok Won Lee, Christian Lupien, Sajan Saini, Tarek Saab, Gianni Taraschi, and Johan van Lierop for all the great times. As well, I would like to thank the other members in the group, Graham Cross, Philip LeBlanc, Yanzhang Liu, Minming Gu, Andre Schirmeisen and Rahma Tabti for their assistance and friendship.

Finally, I would like to thank my parents and my sister, for their love and support.

# 1

# Introduction

The Scanning Probe Microscopy (SPM) group at McGill University was started in 1993 by Dr. Peter Grütter. Over the past four years, we have worked towards the design, construction, and operation of various types of microscopes, which permit the investigation of matter on an atomic scale. One of these microscopes, the Atomic Force Microscope (AFM), probes these dimensions, much smaller than the wavelength of visible light, through the use of a tiny, ultra-sharp tip mounted on a flexible cantilever beam. Interatomic forces, which occur between the atoms of this tip and the atoms of a sample, result in very small deflections of the cantilever beam, which are easily measured using any of several different techniques. These tip-sample interactions allow us to measure various characteristics of our sample, including topography, magnetic structure, frictional forces, adhesion and elasticity.

The purpose of this thesis is to report on the design and characteristics of an Atomic Force Microscope built to operate at liquid helium temperatures. Operating the instrument at 4.2 Kelvin yields several advantages over existing "room temperature" microscopes, including: (i) an increase in sensitivity by more than an order of magnitude[1]; (ii) it allows for the use of an 8 Tesla superconducting magnet; (iii) it permits for the investigation of certain physical phenomena which are observable only at low temperatures. In particular, we hope to use magnetically coated force sensors to measure magnetic interactions between tip and sample, in a technique known as

[1] The sensitivity of our existing "room temperature" Atomic Force Microscope is thermally limited. Please see [1] for details.

Magnetic Force Microscopy (see Section 2.3.3).

In addition to the construction of the microscope, we have initiated a collaboration with a microfabrication group at the University of Sherbrooke, headed by Dr. Jacques Beauvais. At present, this effort has resulted in the production of several calibration grids of varying dimensions(see Figure 2.2), with which tests may be performed during the initial comissioning of the instrument. In the future, we hope to microfabricate several different kinds of samples, including arrays of single domain Permalloy rectangles, with which to investigate magnetic switching (see Chapter 4).

# 2

# Scanning Probe Microscopy & The Atomic Force Microscope

The field of Scanning Probe Microscopy (SPM) began in 1982, with the birth of the Scanning Tunneling Microscope (STM) [2]. This device, invented at IBM Zurich by Gerd Binnig and Heinrich Rohrer, measured the quantum mechanical tunneling current which flows between a sharp conducting tip in close proximity to a conductive sample. For the first time, this instrument allowed one to "see" individual atoms. Although it has become a widely used tool for both imaging and atomic manipulation, the STM is sensitive only to the electronic structure of atoms. However, other Scanning Probe Microscopes have since been developed, all based on the same principle of a small probing tip interacting with the atoms of a sample. These include the Atomic Force Microscope (AFM)[3], the Magnetic Force Microscope (MFM)[4], and the Scanning Near Field Optical Microscope (SNOM)[5], all of which are operated by our group at McGill University.

The Atomic Force Microscope, schematically illustrated in Figure 2.1, is designed to measure interatomic forces. This is accomplished through the use of a sharp probing tip mounted on a flexible cantilever beam. As the tip is brought into close proximity to a sample, the forces between tip and sample cause the cantilever to deflect. An image is taken as the sample is scanned in a raster-like pattern with respect to the cantilever beam, through the use of a piezo tube (see Section 2.6), upon which the sample sits. The deflections of the cantilever or the z-movement of the piezo are recorded and digitized by a computer as a function of the x and y coordinates. They may then be analyzed off-line and used to produce a computer

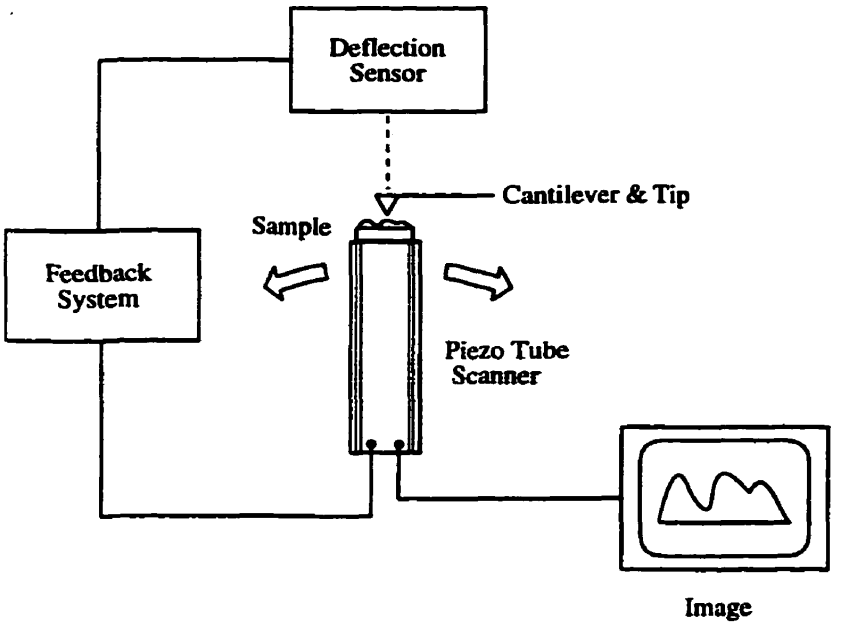


Figure 2.1: The basic principle of an AFM. A sharp probing tip, mounted on a flexible cantilever beam, is scanned over the surface of a sample. Forces between the tip and sample result in cantilever deflections, which are monitored using a deflection sensor. Feedback and computer electronics are used to guide and record the scanning process.

image as shown in Figure 2.2.

## 2.1 *Modes of Imaging and Operation*

The AFM is able to operate in any one of several modes, each of which is sensitive to different forces. This flexibility allows for the investigation of a wide variety of sample characteristics. These different modes of operation can be divided into two groups, known as "imaging" and "operating" modes.

There are two principal imaging modes, known as contact and non-contact. In contact mode, the probing tip is in direct contact with the sample surface. The resulting interaction between tip and sample is dominated by relatively short range ionic repulsion forces, which allow the surface topography to be mapped out with great resolution. Frictional forces may also be investigated under these conditions, using an appropriate deflection sensing mechanism. In non-contact mode, the tip-sample separation varies between 10 and 100 nm. In this regime, forces which include

Figure 2.2: Image of a Au/Pd grid (light lines) on a Si substrate (dark squares). The linewidth is 1 $\mu$m, and the spacing between adjacent lines is 5 $\mu$m. This grid was microfabricated at the University of Sherbrooke.

van der Waals, electrostatic and magnetic forces permit the investigation of such properties as surface topography, distribution of charges, and magnetic domain wall structure.

As with the imaging modes, there are also two operating modes: static mode and dynamic mode, also known as dc- and ac-mode respectively. When operating in the static mode, the cantilever beam bends in response to the force acting between the atoms of the probing tip and the sample. The resulting static deflection is given by Hooke's law,

$$\Delta z = \frac{F_n}{c} \tag{2.1}$$

where $\Delta z$ is the deflection, $F_n$ is the component of the force normal to the cantilever and $c$ is the spring constant of the cantilever.

While in the static mode, the scanning process operates in either of the following ways:

- *Equiforce Mode*: In this case, the force experienced by the cantilever is kept

constant by the use of a feedback loop. This loop monitors the deflection of the cantilever, and controls the tip-sample separation via the piezo tube so as to maintain cantilever deflections at a set value. This mode is the most commonly used.

- *Variable Deflection Mode*: This mode maintains a constant tip-sample separation during the scanning process. The cantilever deflections are measured and may be digitized and stored, resulting in a "force map". In this process the feedback system is not used, enabling higher scan rates.

When used in the second type of operating mode, dynamic mode, the cantilever beam is oscillated at a frequency close to its resonance frequency. The presence of a spatially varying force (and hence a force gradient) will shift the resonance curve by producing an effective spring constant of the cantilever, given by

$$c_{\text{eff}} = c - F' \tag{2.2}$$

with

$$F' = \frac{dF_n}{dn} \tag{2.3}$$

where $d/dn$ is used to indicate the derivative in the direction normal to the plane of the cantilever. In most cases, the cantilever is nearly parallel to the sample, and hence one can make the approximation $F' = \partial F_z/\partial z$.

The resonant frequency of the cantilever in the presence of this force gradient is shifted due to the effective spring constant, according to

$$\omega'_0 = \sqrt{\frac{c_{\text{eff}}}{m}} = \sqrt{\frac{c - F'}{m}} \tag{2.4}$$

where $m$ is an effective mass. For small $F'$ compared with $c$, the binomial expansion gives

$$\omega'_0 = \sqrt{\frac{c}{m}}(1 - \frac{F'}{2c}) = \omega_0(1 - \frac{F'}{2c}) \tag{2.5}$$

where $\omega_0$ is the resonant frequency in the absence of a force gradient. For the case of an attractive force, $F' > 0$, and the resonant frequency will be lowered, such that $\omega'_0 < \omega_0$. For the case of a repulsive force, the opposite is true.

While in dynamic mode, the system is typically operated in constant force gradient mode, whereby the feedback system maintains a constant resonance frequency. This mode of operation is the most common for microscopes equipped with an optical detection system. Of course, the feedback loop may be disabled, and the microscope operated in variable gradient mode, analogous to the situation in static mode.

Varying requirements of instrument sensitivty, depending upon which forces are under investigation, is often a principal reason for choosing one operating mode over another. For example, while operating in the static mode, the sensitivity of the deflection sensor limits the minimum force that can be detected[1]. Typically it is better than 0.01 nm in a 1 kHz bandwidth, corresponding to a minimum detectable force of $F_{min} = 10^{-11}$N using a 1 N/m cantilever. A key reason for operating the microscope in the dynamic mode is its improved sensitivity to long-range forces. For example, a force with a $1/z^2$ dependence is related to its force gradient by $F' = -2F/z$. For typical values of $z = 10$ nm and $F' = 10^{-4}$N/m, which is easily detectable, the force $F = 5 \times 10^{-13}$ N corresponds to a static deflection of only $5 \times 10^{-3}$ Å using a 1 N/m cantilever. This deflection is smaller than can be detected by most systems. An added advantage of the dynamic measurement process is the absence of distortion from lateral forces such as friction.

### 2.1.1 *Measuring the Resonance Frequency Shift of the Cantilever*

Two methods are commonly used to detect the resonance frequency shift resulting from a force gradient. The first method, "slope detection" [6, 7], uses a lock-in amplifier to measure the amplitude or phase of vibration of a cantilever which is driven at a fixed frequency $\omega_d$ by a piezoelectric bimorph (see Section 2.6). The

[1] When operated in contact mode, the resonant frequency of the cantilever is larger than its natural frequency, owing to the fact that one end of the cantilever is no longer free to vibrate. As a result, thermal vibrations of the cantilever (see Section 2.4) are greatly reduced.

amplitude of the cantilever oscillations is chosen to give the tip an amplitude of 1-10 nm. To ensure a monotonic response as the tip is approached to the attractive sample, the driving frequency is chosen to be larger than $\omega_0$, the resonance frequency in the absence of a force gradient.

The steady-state amplitude $A$ of the cantilever vibration depends on the resonance frequency $\omega'_0$ (defined in Eq. 2.4) according to

$$A(\omega'_0) = \frac{A_0(\omega'_0/\omega_d)}{\sqrt{1+Q^2(\omega_d/\omega'_0 - \omega'_0/\omega_d)^2}} \tag{2.6}$$

where $A_0$ is the cantilever amplitude when $\omega'_0 = \omega_d$, and $Q$ is the quality factor of the resonance. To ensure maximum sensitivity to changes in $\omega'_0$, the drive frequency is chosen so that $A(\omega'_0)$ has the steepest slope. In this case, an amplitude change given by

$$\Delta A = (\frac{2A_0Q}{3\sqrt{3}c})F' \tag{2.7}$$

results from a resonance frequency shift due to the force gradient $F'$. This is illustrated in Figure 2.3. While it is clear that increasing the $Q$ factor maximizes sensitivity, it also restricts the bandwidth of the system. This is because the expression for the amplitude contains a transient decay term, with a time constant linear in $Q$. Hence, the slope detection mechanism is unsuitable for most vacuum applications, where large $Q$ factors reduce the bandwidth to an unacceptable level [8].

The second detection method uses frequency modulation (FM) to directly observe the resonance frequency shift due to $F'$ [8]. In this case, a high-$Q$ cantilever oscillating at resonance becomes the frequency determining element of an oscillator. The oscillation of the cantilever is maintained by a positive feedback loop using the signal from the deflection sensor. The amplitude of the oscillation is controlled by an amplifier with automatic gain control. Any change in $F'$ causes an instantaneous change in the frequency of oscillation, which is then measured by a phase lock loop. Please see [8] for more details.

Assuming that thermal vibrations of the cantilever beam are the limiting noise

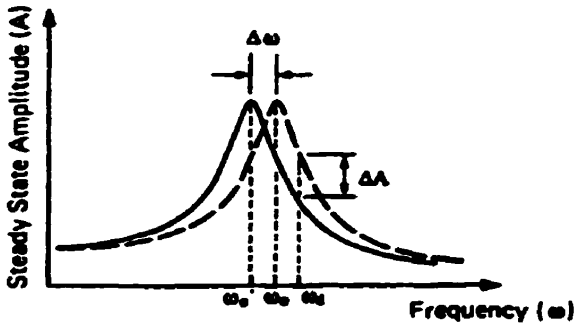


Figure 2.3: In a slope detection system, the cantilever beam is oscillated at a frequency $\omega_d$, slightly off resonance. A change in the force gradient causes the resonant frequency to shift from $\omega_0$ to $\omega'_0$, resulting in a change, $\Delta A$, in the steady-state amplitude. From [8].

source, the minimum detectable force gradients of the two methods are within a factor of $\sqrt{2}$ of each other [8, 9], with the value for FM detection given by

$$F'_{\text{min}} = \frac{1}{A}\sqrt{\frac{4ck_{\text{B}}TB}{\omega_0 Q}} \tag{2.8}$$

where $A$ is the rms amplitude of the cantilever oscillation, $B$ is the detection bandwidth, $T$ is the temperature in Kelvin, and $k_{\text{B}}$ is Boltzmann's constant. Contrary to the case of slope detection, here $Q$ depends only on the damping of the cantilever beam, and $B$ is set only by the characteristics of the FM demodulator. Hence, FM detection allows the sensitivity to be increased by using a very high $Q$ without sacrificing bandwidth or dynamic range.

According to Eq. 2.8, there are a number of parameters one can optimize in order to improve sensitivity: (i) it is clear that for the case of a thermally limited system, operating at 4 Kelvin as opposed to room temperature yields an improvement in the minimum detectable force gradient by about an order of magnitude; (ii) the combined requirements of a low spring constant and a high resonant frequency are needed in order to minimize $\sqrt{c/\omega_0}$, which is achieved through the use of microfabricated cantilevers (see Section 2.4); (iii) the $Q$ factor of the system should be made as large as possible. One way to achieve this is to oscillate the cantilever beam at a higher flexural mode, for example the second or third harmonic of the cantilever's resonance

frequency. This technique is discussed in [10]. Other parameters which effect the $Q$ factor include the environment and mounting of the cantilever beam, both of which were investigated by one of the summer students working in our group.

It was found that an increase of the $Q$ factor by a factor of about 100 results when the cantilevers are placed in vacuum, as opposed to cantilevers in air. This is due to the absence of viscous air damping which would otherwise result in some energy loss. Plotted in Figures 2.4 and 2.5 is the log of the $Q$ factor versus resonance frequency for a number of commercially available, routinely used cantilever beams (see section 2.4). Figure 2.4 illustrates measurements done in air, while Figure 2.5 are for those done under vacuum. The $Q$ factor in air generally follows an exponential relation while in vacuum it seems that the $Q$ factor is not a function of the resonance frequency.

The data illustrated in Figures 2.4 and 2.5 used cantilevers mounted using silver paint. A different mounting scheme, using three ruby balls in the form of a three point mount, was also investigated. It was found that by using the balls, the ratio of the $Q$ factor in vacuum to that in air increased to 130 and 170 in two separate trials, from a value of 80 using the silver paint. This increase in $Q$ factor is the result of a reduced contact area between the cantilever and the mount, which thereby minimizes the amount of energy transfered to the mount. Although a difference in $Q$ factor does result, it is relatively small in comparison to the change produced by operating in vacuum.

Results of these investigations are listed in Table 2.1. Note in particular that since the minimum force gradient detectable under thermally limiting conditions is proportional to $\sqrt{c/\omega_0 Q}$, as given in Eq. 2.8, a cantilever with a higher spring constant $c$ may still be more "sensitive" owing to a higher $Q$ value, than a cantilever with a lower spring constant.

## 2.2 *Force-Distance Curves*

While in contact mode, the interactions between the tip and the sample can be schematically represented using a force-distance curve. These plots indicate graphi-

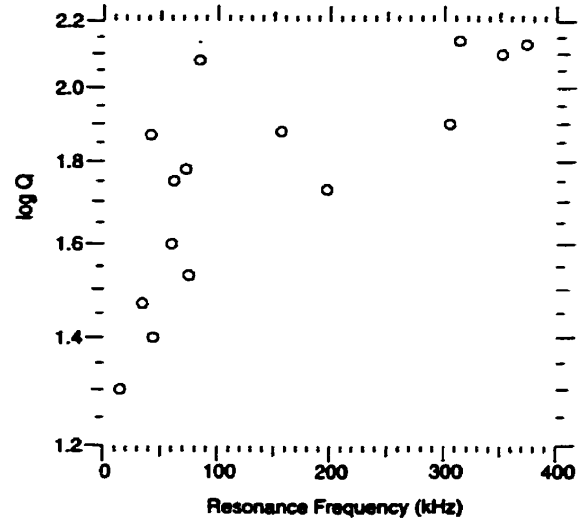


Figure 2.4: The logarithm of the $Q$ factor is plotted versus cantilever resonance frequency, as measured in air. Note the increase in Log Q as the resonance frequency increases. From [11].

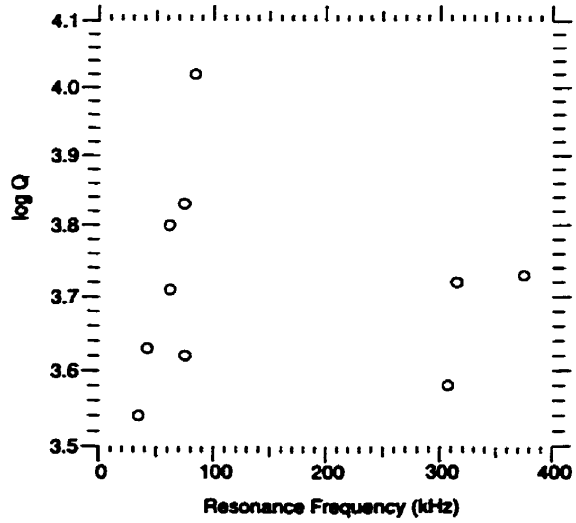


Figure 2.5: The logarithm of the $Q$ factor is plotted versus cantilever resonance frequency, as measured in vacuum. There appears to be no functional dependence of the $Q$ factor on the resonance frequency. From [11].

| Cantilever | $c$ (N/m) | $\omega_0$ (kHz) air | $\omega_0$ (kHz) vacuum | $\sqrt{\frac{c}{\omega_0 Q}} \times 10^{-5}$ air | $\sqrt{\frac{c}{\omega_0 Q}} \times 10^{-5}$ vacuum |
|---|---|---|---|---|---|
| A | 1.9 | 60 | 62 | 90 | 7.7 |
| B | 2.8 | 72 | 74 | 90 | 7.4 |
| C | 13 | 313 | 314.7 | 60 | 11 |
| D | 18 | 373.5 | 375 | 60 | 9 |
| E | 0.16 | 34.4 | 34.7 | 40 | 3.6 |
| F | 0.24 | 41.4 | 42.3 | 28 | 3.7 |
| G | 0.32 | 15 | 15 | 54 | 6 |
| H | 0.06 | 44 | 44 | 45 | 5 |
| I | 2.8 | 83.7 | 84 | 52 | 6 |

Table 2.1: Cantilever beam sensitivities of various cantilevers, denoted A through I. The important value is that listed in the two last columns, which is proportional to the minimum force gradient measurable in a thermally limited system. From [11].

cally the force experienced by the tip as a function of tip-sample separation.

An example of a force-distance curve is illustrated in Figure 2.6. As the sample is approached towards the tip (region A), the cantilever bends towards the sample due to the attractive van der Waals force. At B, the gradient of the attractive force exceeds the spring constant $c$ of the cantilever, causing the cantilever to "snap" into the sample surface. This is usually due to surface tension attraction (see Section 2.3.4). As the tip-sample distance is further decreased, the cantilever enters a repulsive regime, where forces from the sample push the lever away (region C). As the sample is retracted, the tip continues to stick to the surface (region D), until it jumps out of contact at E.

## 2.3 *Forces Measured by AFM*

A variety of forces can be investigated using the Atomic Force Microscope. The following sections provide a brief review.

### 2.3.1 *Van der Waals Forces*

Van der Waals forces arise due to the instantaneous polarization of atoms, which then interact through dipole-dipole interactions with surrounding atoms. These forces are

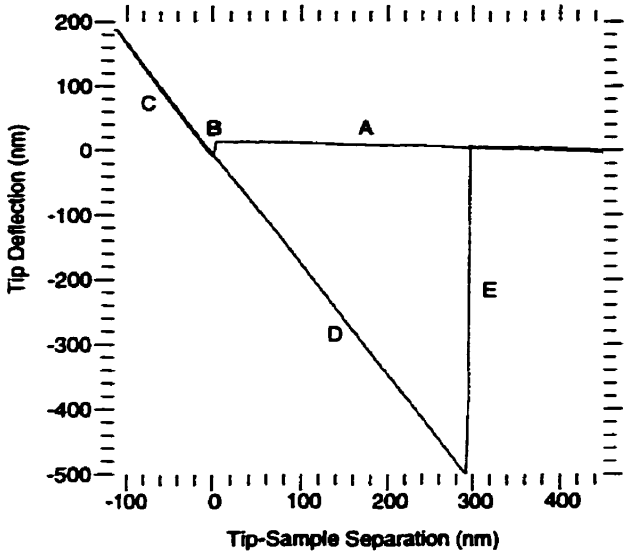


Figure 2.6: A force-distance curve illustrating the deflection experienced by the cantilever beam as a function of tip-sample separation. Numerical values of the force acting on the cantilever are obtained by multiplying the cantilever's deflection by its spring constant. The data was taken using the sample illustrated in Figure 2.2.

present in all force microscope experiments, though they are exceedingly weak and fall off rapidly with distance; the attractive van der Waals force between atoms is proportional to $1/r^7$, where $r$ is the separation distance. Though their range is limited, this force is effective for distances of a few Ångstroms to a few hundred Ångstroms, and can be used to measure topography with a resolution of a few nm [7, 12].

### 2.3.2 *Electrostatic Forces*

The force between a conductive tip and a charge distribution on an insulating sample is given by

$$F_{\text{charge}} = q_{\text{tip}} E_z \tag{2.9}$$

where $q_{\text{tip}}$ is the charge induced on the tip, and $E_z$ is the z component of the electric field, due to the charge distribution on the sample (the x and y components of this electric field twist the cantilever, but do not cause vertical deflections). The induced charge, $q_{\text{tip}}$, is comprised of two terms; the first, $q_{\text{surface}}$, is the charge induced on the

tip by the sample charge distribution, and the second, $C \cdot V$, results from an external voltage $V$ which is applied across the tip-sample separation, with corresponding capacitance $C$. This gives

$$q_{\text{tip}} = -(q_{\text{surface}} + C \cdot V) \tag{2.10}$$

The resulting capacitive force,

$$\begin{aligned} F_{\text{capacitive}} &= \frac{1}{2}\frac{\partial(CV^2)}{\partial z} \\ &= 1/2C'V^2 \end{aligned} \tag{2.11}$$

where $C'$ is the derivative of the capacitance in the z direction, also contributes to the total force, which is then given by

$$F_{\text{total}} = -(q_{\text{surface}} + C \cdot V)E_z + 1/2C'V^2 \tag{2.12}$$

To a first approximation, $E_z$ is proportional to the charge on the sample. The first two terms, therefore, are indicative of the charge distribution. The total electrostatic force can easily be modified using the applied voltage, in order to distinguish it from other forces, such as van der Waals forces or magnetic forces. As well, when the voltage is modulated sinusoidally with angular frequency $\omega$, the capacitive contribution can be measured as an ac signal of frequency $2\omega$, whereas the charge contribution is measured as a dc signal and as a signal of frequency $\omega$ [13].

### 2.3.3 *Magnetic Forces*

The stray magnetic field emanating from the surface of a magnetic sample produces a force on a nearby magnetic tip. If one approximates the tip as a point dipole, the force $\mathbf{F}$ acting upon it is given by

$$\mathbf{F} = \nabla(\mathbf{m} \cdot \mathbf{H}) \tag{2.13}$$

where $\mathbf{m}$ is the magnetic moment of the tip and $\mathbf{H}$ is the magnetic field from the sample. In reality, the total force must be found by integrating Eq. 2.13 over all of the magnetic dipole moments within the tip.

The magnetic field from one magnetic particle, of magnetization $\mathbf{m}_1$, felt by another magnetic particle, of magnetization $\mathbf{m}_2$, a distance $\mathbf{r}$ away, is given by

$$\mathbf{H}(\mathbf{r}) = \frac{3\hat{\mathbf{r}}(\hat{\mathbf{r}} \cdot \mathbf{m}_1) - \mathbf{m}_1}{r^3} \tag{2.14}$$

where $\hat{\mathbf{r}}$ is the unit vector in the $\mathbf{r}$ direction. The corresponding force is then given by

$$\mathbf{F} = \nabla \left( \frac{3(\mathbf{m}_1 \cdot \hat{\mathbf{r}})(\mathbf{m}_2 \cdot \hat{\mathbf{r}}) - \mathbf{m}_1 \cdot \mathbf{m}_2}{r^3} \right) \tag{2.15}$$

The technique known as Magnetic Force Microscopy (MFM) measures the magnetostatic interactions arising from the magnetic dipoles in the tip interacting with the dipoles in a sample, according to Eqs. 2.14 and 2.15. These interactions are long ranged, and are typically sensed at tip-sample separations greater than 10 nm while operating the microscope in the ac mode.

The total magnetic force acting between tip and sample can be found either by summing the forces acting between each dipole in the tip and each dipole in the sample, or alternatively, by using Eq. 2.13 summed over the dipoles in the tip, using a calculated field value from the sample, according to

$$\mathbf{F}_{\text{magnetic}} = \int_{\text{tip}} \nabla_{\mathbf{r}} (\mathbf{M}(\mathbf{r}') \cdot \mathbf{H}(\mathbf{r} + \mathbf{r}')) dV' \tag{2.16}$$

where $\mathbf{M}(\mathbf{r}')$ is the magnetization of the volume element of the tip and $\mathbf{H}(\mathbf{r} + \mathbf{r}')$ is the stray field from the sample.

It is generally assumed for hard magnetic materials that during the scanning process the sample magnetization is unaffected by the field from the tip. However, soft magnetic materials are more susceptible to unwanted perturbations from the tip stray field. Please see [4] for more details.

### *2.3.4 Capillary Forces*

When force measurements are performed under ambient conditions, the presence of vapours, particularly water vapours, leads to capillary forces. Typically, these arise

due to the thin film which tends to cover the sample surface, forming a meniscus which strongly draws the tip towards the sample. The resulting force is given by [13]

$$F_{\text{Capillary}} = \frac{\gamma 2\pi R d(r_1 + r_2)}{r_1 r_2} \tag{2.17}$$

where $\gamma$ is the surface tension, $R$ is the tip radius, $d$ is the tip penetration depth into the liquid, and $r_1$ and $r_2$ are the radii of the meniscus.

Capillary forces are much larger than van der Waals forces at small tip-sample separations, and significantly effect contact mode imaging [13]. For example, the strong attractive capillary force exerted on the cantilever by surface monolayers, which typically include the presence of lubricants and contaminants, as well as the thin water layer often present when operating in air, cause "snap-back" points on the force-distance curve. This phenomenon was evident in Figure 2.6, and is illustrated specifically in Figure 2.7. In order to avoid these effects, imaging may be performed within a liquid cell. These cells are small, leak-tight containers, housing both the sample and the cantilever beam. A liquid, water for example, may be injected into this volume, fully immersing both the sample and the cantilever and thereby eliminating the capillary forces.

### 2.3.5 *Ionic Repulsion Forces*

When the tip and the sample are in contact, short ranged forces act to prevent tip penetration into the sample. These repulsion forces arise due to the Pauli exclusion principle, which prevents electrons from occupying identical states, and from Coulombic repulsion between incompletely screened nuclei of tip and sample atoms. Though large in magnitude, these forces have a very limited range, decaying within tenths of an Ångstrom. These forces may be used to investigate atomic-scale topography of the sample while operating in contact mode.

### 2.3.6 *Frictional Forces*

While operating in contact mode, frictional forces can arise as the tip is scanned across the sample surface. These forces can be investigated by measuring the torque

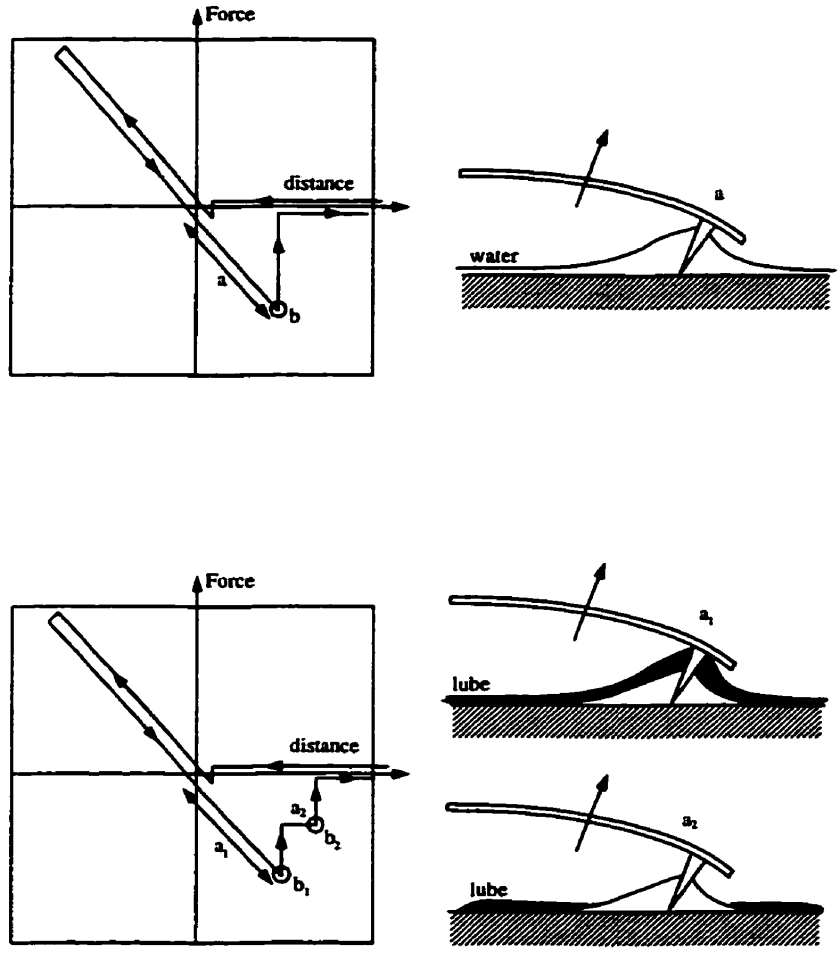


Figure 2.7: Force vs. distance curves in the presence of (i) a water monolayer (top) and (ii) a lubrication layer (bottom). In (i), as the cantilever is pulled away from the sample, the water layer continues to hold the tip in contact with the surface, bending the cantilever as a result (region a). At some point the cantilever will snap free; this is known as the snap-back point (point b). If a lubrication layer is present, as in (ii), multiple snap-back points can occur, the positions and amplitudes of which are dependent on the viscosity and thickness of the layers present. Adapted from [14].

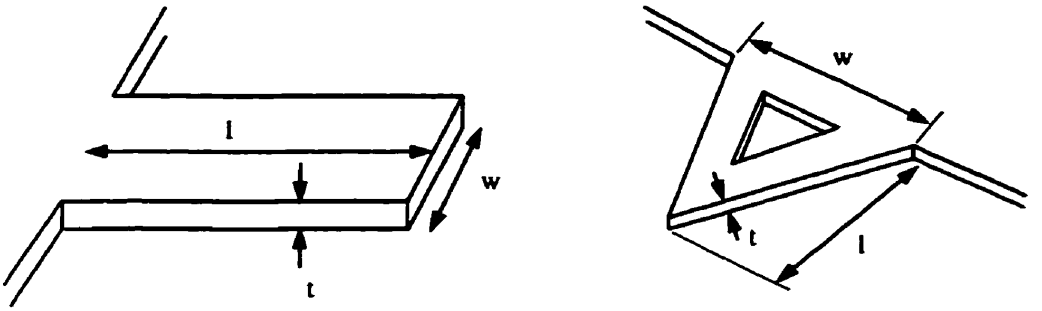


Figure 2.8: Schematic diagrams of rectangular and triangular cantilever beams, indicating the length (l), width (w), and thickness (t).

of a cantilever during the scanning process. To do this, a laser beam deflection system is used, in conjunction with a four-quadrant photodetector. While the difference between the upper and lower quadrants is proportional to vertical cantilever deflection, the difference between the left and right quadrants is proportional to torsion arising from friction between the sample surface and the cantilever. While it is difficult to obtain quantitative values, owing to a number of ill-defined parameters, such as true contact area and tip geometry, the technique is well suited to find relative variations on a local scale.

## 2.4 Force Sensors

Most force microscopes today use batch microfabricated cantilevers, which are widely available from several companies. Two materials, Si and $Si_3N_4$, are commonly used, producing cantilevers with either a rectangular or a triangular "V-shaped" geometry [15]. These are illustrated in Figure 2.8. Cantilevers for use in MFM are produced by coating batch fabricated silicon cantilevers with thin magnetic films, often Co, CoPtCr, or NiFe [4]. Both Si and $Si_3N_4$ cantilevers are available with integrated tips.

Cantilever beams are characterized in part by their spring constant, $c$, which depends strongly on the length and thickness of the cantilever, as well as the elastic modulus of the cantilever material. Cantilevers with low spring constants, known as

"soft cantilevers", experience measurable deflections when acted upon by very small forces, whereas cantilevers with larger spring constants require larger forces in order to produce equivalent deflections. In order to effectively probe small forces, it is therefore necessary that spring constants should be made as small as possible. However, a lower limit to $c$ is imposed due to thermal excitations. Using the equipartition theorem, a cantilever of spring constant $c$ will experience thermal vibrations with an rms amplitude $A$ of [4]

$$A = \sqrt{k_B T / c} \tag{2.18}$$

where $k_B$ is Boltzmann's constant and $T$ is the temperature in Kelvin. For a 1 N/m cantilever at room temperature, the thermal vibration amplitude is about 0.6 Å, which is easily detectable. Operation of the system at liquid helium temperatures however, provides a decrease in thermal vibrations by an order of magnitude.

In addition to the spring constant, the other important quantifiable property of the cantilever beam is its resonance frequency. Cantilevers with a high resonance frequency are desirable, because they are insensitive to acoustic noise and external vibrations (see Section 3.6). For the case of a rectangular cantilever beam of thickness $t$, length $l$, mass density $\rho$ and Young's modulus $E$, the lowest resonance frequency (that is, the first eigenfrequency) is given by [12]

$$\begin{aligned} f &= \frac{(1.8751)^2}{2\pi} \frac{t}{l^2} \left(\frac{E}{12\rho}\right)^{1/2} \\ &= \frac{(1.8751)^2}{2\pi\sqrt{3}} \sqrt{c/m} \end{aligned} \tag{2.19}$$

The second part of the equation expresses the resonance frequency in terms of the spring constant $c$ and mass $m$. From Eq. 2.19, it is clear that in order to maintain a large resonance frequency with a small spring constant, the mass must be reduced as well. Therefore, the dimensions of the cantilever should be chosen to be as small as possible. Typical dimensions are a few hundred micrometers in length, with a thickness or order 1 $\mu$m.

In contrast to the rectangular cantilever, the more complicated geometry of the triangular cantilever does not allow for exact solutions to the differential equation describing its motion, from which its resonance frequency might be extracted. However, variational method calculations for the resonance frequencies of commercial Si and $Si_3N_4$ triangular cantilevers can be found in [16].

## 2.5 *Cantilever Deflection Measurement Techniques*

There are various methods commonly used to measure the cantilever deflections arising from tip-sample interactions. These include:

- *Electron Tunneling*: Used in the original AFM, electron tunneling incorporates an STM to measure the tunneling current between the STM tip and the conductive back side of a cantilever. This technique is very sensitive - a change in the STM tip-cantilever distance of an Ångstrom corresponds to a change in the tunneling current by an order of magnitude, allowing one to achieve a resolution of 0.01 Å in a bandwidth of a few kHz [12]. Limitations of this technique include the fact that the tunneling current can depend on the roughness of the back side of the cantilever, leading to distortions of the image; the cantilever must be conducting, and be reasonably free of contamination so as to ensure a good tunnel junction; and the interaction between the STM tip and the cantilever is not negligible, and leads to forces of the order $10^{-9}$ N [17, 18].

- *Optical Detection*: This method is currently the most widely used method in force microscopy, and has several distinct advantages over the Electron Tunneling method. These include a negligible interaction between the laser beam and the cantilever; the capability of measuring deflections on the order of 0.1 Å within a detection bandwidth of dc to 10 kHz [19], and an insensitivity to the roughness of the back of the cantilever, owing to the large laser beam size. As well, optical techniques work for cantilever deflections in excess of 100 nm,

whereas electron tunneling is restricted to motion less than 1 nm. There are two classes of optical detection: interferometry [9] and beam deflection [20, 21].

  - *Optical Interferometry*: This technique, used in both our room temperature and low temperature instruments, uses an optical fibre to reflect laser light off of the back side of a cantilever. Deflections are measured using the interference pattern generated from the cavity formed by the reflective back side of the cantilever and the cleaved end of the optical fibre. A sensitivity of $10^{-4}$ Å/$\sqrt{\text{Hz}}$ is typically achieved [22]. See Section 3.7.1 for more details.
  - *Laser Beam Deflection*: In this technique, a laser beam is reflected off the back side of a cantilever, and directed towards a position-sensitive detector, most often a four quadrant photodetector. This technique allows for the measurement of lateral deflections of the cantilever, such as those caused by surface friction.

- *Capacitance*: In this technique, a sensor and the back side of the cantilever beam form the two plates of a parallel plate capacitor, the capacitance of which is inversely proportional to their separation. Therefore, a small change of separation distance will cause a change in capacitance. At a mean separation of 1 $\mu$m, a change of 0.1 Å causes a relative variation of $10^{-5}$, which is comparable to the optical methods [13]. Unfortunately, the sensor may exert a large force (and force gradient) on the lever, causing the cantilever to snap-in to the capacitor plate. As well, this technique requires that the cantilever beam be somewhat conducting.

- *Piezoresistive Cantilever*: This technique uses cantilevers fabricated from piezoresistive material, the resistance of which changes when subjected to a mechanical stress. The deflection measurement is then easily read as a change in the cantilever resistance. Please see [23] for more details.

## 2.6 Piezoelectrics

Piezoelectric materials are used in several key components of the AFM. Specifications of particular components used in our system are found in Chapter 3. A general overview of the piezoelectric effect and related details is presented below.

The piezoelectric effect, discovered in 1880 by Pierre and Jacques Curie, is a property of certain classes of crystalline materials which contain no inversion symmetry in their point group [24]. If a mechanical pressure is applied to one of these materials, a voltage proportional to the applied pressure is produced. Conversely, an applied electric field causes the material to experience dimensional changes. Referring to Figure 2.9, when a voltage $V$ is applied to a rectangular piezoelectric material, the electric field $E$ in the $z$ direction is then given by

$$E_3 = \frac{V}{z} \tag{2.20}$$

In this notation, the x, y, and z axes are denoted by 1, 2 and 3 respectively. The electric field gives rise to a strain $\Delta L/L$, the magnitude and direction of which is characterized by a strain tensor. For example, the $xx$ component of this tensor is

$$S_1 \equiv \frac{\delta x}{x} \tag{2.21}$$

and the $zz$ component is

$$S_3 \equiv \frac{\delta z}{z} \tag{2.22}$$

where the $\delta$ represents the change in the respective dimension. Piezoelectric coefficients are defined as the ratio of the strain components divided by the applied electric field magnitude. For example,

$$d_{31} \equiv \frac{S_1}{E_3} \tag{2.23}$$

and

$$d_{33} \equiv \frac{S_3}{E_3} \tag{2.24}$$

The piezoelectric coefficients have dimensions of meters/volt in the SI units, and owing to their extremely small values, are often quoted in SPM literature in units of Å/V.

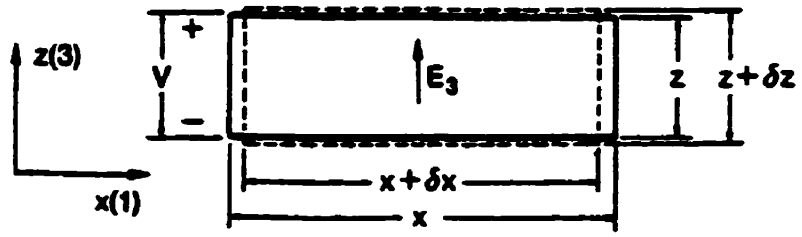


Figure 2.9: A voltage applied in the $z$ direction to the rectangular piezo of piezoelectric material gives rise to a strain in both the $z$ and the $x$ directions. From [25].

While piezoelectric properties occur naturally in some crystalline materials, most contemporary applications utilize polycrystalline ceramics, in which piezoelectric properties can be induced. These ceramics are easily manufactured into various shapes and sizes which can be tailored to specific applications.

The piezoelectric materials most commonly used in SPM applications are lead zirconate titanate ceramics, also known as PZT. These ceramics are polycrystalline, with each crystal possessing its own dipole moment. Initially, the dipole moments are randomly aligned, and hence the material exhibits no macroscopic piezoelectric effect. A poling process is used in order to produce a permanent electric polarization. This process involves the application of an electric field while the temperature of the material is held above its Curie point, the characteristic temperature above which the piezoelectric property is lost. The dipoles are aligned with the poling field, thereby creating a macroscopically anisotropic piezoelectric material. By convention, the direction of the poling field is labeled as the 3 or positive $z$ direction.

An applied voltage with the same polarity as the poling voltage causes an expansion along the poling axis and contraction perpendicular to the poling axis. A voltage with the opposite polarity produces the opposite effect. Conversely, a voltage with the same polarity as the poling voltage results from a compressive force applied parallel to the poling axis, or from a tensile force applied perpendicular to the poling axis.

There are several additional parameters which distinguish between the different

PZT ceramics. These include:

- *Curie Temperature*: An irreversible degradation of the piezoelectric property occurs if the material is heated above this temperature. At temperatures close to but still lower than the Curie temperature, serious degradation may occur. Typical specified maximum operating temperatures for piezoelectric materials are much lower than its Curie point. Each ceramic composition has its own Curie point.

- *Temperature Dependence of Piezoelectric Coefficients*: Certain piezoelectric coefficients exhibit a variation with temperature. The variation differs for different PZT materials. Figure 2.10 illustrates measured variations with temperature of $d_{31}$ for several commonly used PZT materials.

- *Depoling Field*: If a strong electric field is applied to the piezoelectric material in a direction other than that used in the poling process, the piezoelectric properties of the material become altered or lost.

- *Coupling Constants*: The electromechanical coupling constant $k$ is defined as the ratio of the electrical energy converted into mechanical energy to the input electric energy. In other words, it characterizes the efficiency of energy conversion between mechanical and electrical forms. The values for PZT are the highest amongst all piezoelectric materials.

- *Aging*: The piezoelectric effect of polycrystalline ceramics decays logarithmically with time after poling. The rate of aging of various properties depends on the particular ceramic composition, as well as the way the ceramic is processed during manufacture. The aging process can be accelerated by exposure to one or a combination of either: (i) high mechanical stress; (ii) strong electric depoling field; (iii) high temperatures approaching the Curie temperature. Because of aging, exact values of various piezoelectric constants may only be specified

for a standard time after poling. The longer the time period after poling, the more stable the material becomes.

Table 2.2 lists some parameters of several PZT materials.

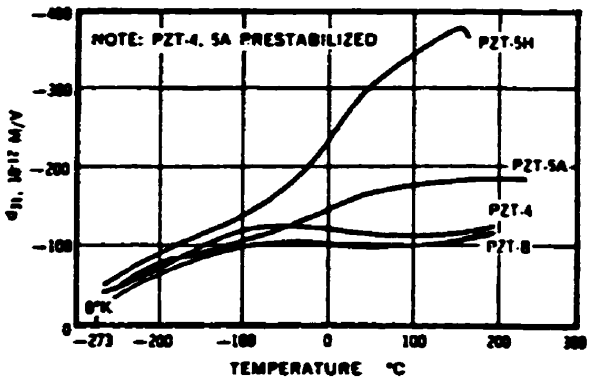


Figure 2.10: The variation of the piezoelectric coefficient $d_{31}$ with temperature is shown for several PZT materials. From [26].

| Material Properties | PZT-4 | PZT-4D | PZT-5A | PZT-5H | PZT-8 |
|---|---|---|---|---|---|
| $d_{31}$Å/V @ 293 K | -1.27 | -1.35 | -1.73 | -2.62 | -0.95 |
| $d_{33}$Å/V @ 293 K | 2.95 | 3.15 | 3.80 | 5.83 | 2.20 |
| $d_{31}$Å/V @ 4.2 K | — | — | -0.31 | -0.33 | — |
| $d_{33}$Å/V @ 4.2 K | — | — | 0.69 | 0.74 | — |
| Curie Temperature °C | 320 | 320 | 350 | 190 | 300 |
| AC depoling field kV/cm rms | 10 | 10 | 7 | 4 | 15 |
| Young's modulus $10^{10}$N/m$^2$ | 8.1 | 7.5 | 6.3 | 6.3 | 8.5 |
| Thermal conductivity W/m°C | 2.1 | 2.1 | 1.5 | 1.5 | 2.1 |
| Density g/cm$^3$ | 7.5 | 7.6 | 7.5 | 7.45 | 7.5 |

Table 2.2: Some important properties of PZT ceramics. From [27].

### 2.6.1 *The Bimorph*

The cantilever beam is mounted on a special arrangement of piezoelectric material, known as a bimorph. This device is composed of two thin plates of piezoelectric material glued together. An applied voltage causes one plate to expand and the other

to contract, flexing the entire assembly, and producing a relatively large displacement. A dc voltage may be applied to the bimorph in order to adjust the position the cantilever beam with respect to the optical fibre, thereby "fine tuning" the interference pattern. The application of a sinusoidally varying voltage to the bimorph is necessary to operate the microscope in ac mode (see Section 2.1). For a detailed treatment of the bimorph, please see [25].

### 2.6.2 *Tube Scanner*

The tube scanner is the device upon which the sample is mounted, and is used in order to raster scan the sample with respect to the probing tip. The basic design is that of a tube made of PZT, polarized in the radial direction, and with electrodes on the outer and inner surfaces. The outside electrode is axially segmented into four quadrants.

In our system, the inner electrode is connected to the $z$ voltage, while opposite quadrants are connected to $+$ and $-$ $x$ and $y$ voltages. That is, voltages $+V_x$ and $-V_x$ are applied to opposite $x$ quadrants, and voltages $+V_y$ and $-V_y$ are applied to opposite $y$ quadrants. For the case of equal and opposite voltages applied to opposite quadrants, the scan ranges $\Delta x$ and $\Delta y$ are then given by [27]

$$\Delta x, y = \frac{0.9 d_{31} V L^2}{d_{\mathrm{m}} t} \tag{2.25}$$

where $V$ is the applied voltage, $L$ is the length of the tube, $d_{\mathrm{m}}$ is the mean diameter of the tube, given by $d_{\mathrm{m}}$=(OD + ID)/2 with OD and ID being the outer- and inner-diameters respectively, and $t$ is the wall thickness of the piezo tube. The $z$ range is given by

$$\Delta z = \frac{d_{31} V L}{t} \tag{2.26}$$

For a detailed treatment of piezo tubes, please see [25].

### 2.6.3 *Nonlinearities of Piezoelectrics*

Piezoelectric materials exhibit several nonlinear effects, which tend to distort the image during the scanning process. These effects, as they apply to the piezo tube,

include:

- *Intrinsic Nonlinearity:* Strain varies linearly with applied electric field, as per Eqs. 2.23 and 2.24 for example, only to a first approximation [14]. The result of this intrinsic non-linear behavior is that periodic structures will show non-uniform spacings, and linear objects will appear curved. This phenomenon can be seen in Figure 2.2, producing diamond shaped instead of square regions.

- *Hysteresis:* The extension of the piezoelectric material is not single valued with applied voltage, but rather depends on whether the material is expanding or contracting. As a result, data are usually collected only in one scan direction. Hysteresis in the direction perpendicular to the plane of the sample results in erroneous height profiles.

- *Creep:* The mechanical response of the piezoelectric material does not instantaneously follow the applied voltage. Rather, dimensional changes occur in two steps. The first step, which contributes the majority of the change, takes place quickly, in less than a millisecond. The second step occurs over a much longer time scale, on the order of 10 to 100 seconds, and produces a much smaller displacement. The ratio of the second dimensional change to the first provides a quantitative measure of the effect, and is typically between 1% and 20% [14]. Creep is most noticeable when a voltage offset is applied to the piezo tube, in order to move to a different region of interest, causing the imaging area to slowly drift for several minutes.

- *Cross Coupling:* Movement in the x-axis or y-axis direction produces a spurious motion in the z-axis direction, called cross coupling, which produces a bowl-shaped image of a flat surface. Sources of this effect include: the tensor nature of the strain fields, the fact that the electric field is not uniform across the piezo tube, the existence of "cross talk" between x, y and z electrodes, and the fact that, by nature of its geometry, the piezo tube scans in an arc, not in a plane.

# 3

# Instrumentation

Illustrated in Figure 3.1 is a schematic overview of the general instrument, including the dewar, cryostat, superconducting magnet, as well as the vacuum can and its contents. Figure 3.2 shows the vacuum can contents in detail. The following sections discuss the different components of the instrument.

## *3.1 Dewar*

Invented in the late nineteenth century by Sir James Dewar [28], the dewar is a double-walled insulated container, similar to a common coffee thermos, which houses the experiment and serves to isolate it from the relatively hot environment of the laboratory. The defining principle behind its operation is this: the lowest thermal conductivity material that can be used to separate two thermal reservoirs is in fact no material at all. Hence, a vacuum is used to separate the inner and outer walls of the container.

For two reservoirs separated by a vacuum, the applicable method of heat transport is thermal radiation. This is described in terms of black body radiation, and employs the Stephan-Boltzmann relation,

$$\dot{Q} = \sigma \epsilon A T^4 \tag{3.1}$$

where $\dot{Q}$ is the amount of heat radiated, $\sigma$ is the Stephan-Boltzmann constant, $\epsilon$ is the emissivity of the material, $A$ is the available surface area for heat radiation and $T$ is the temperature in Kelvin. Making the simplifying assumptions that the emissivity

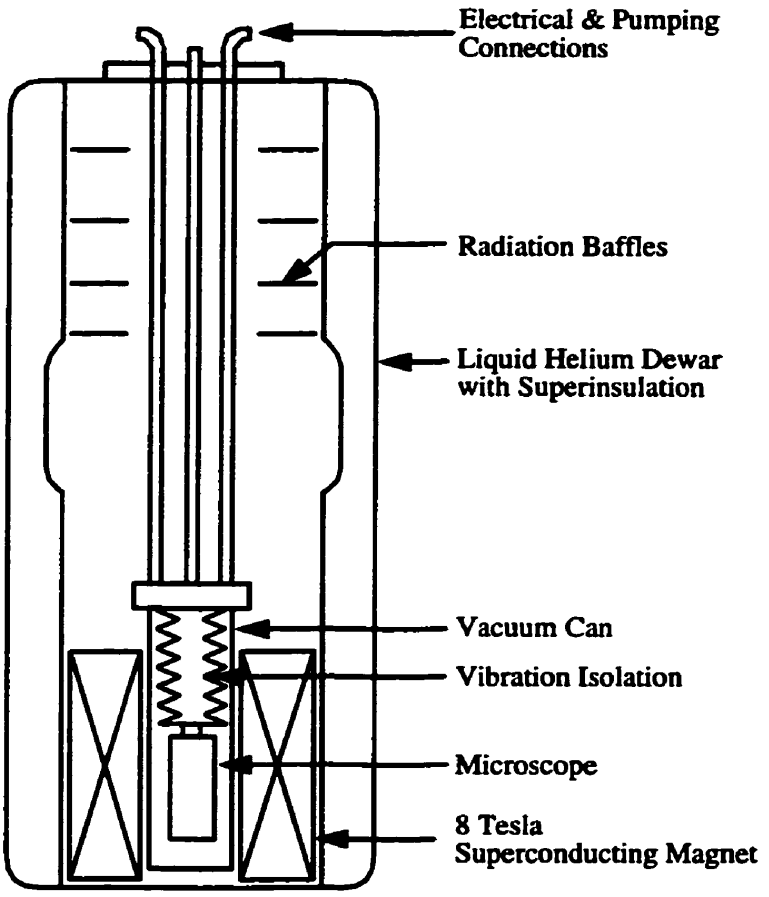


Figure 3.1: Schematic representation of the general instrument, including the microscope and low temperature components.

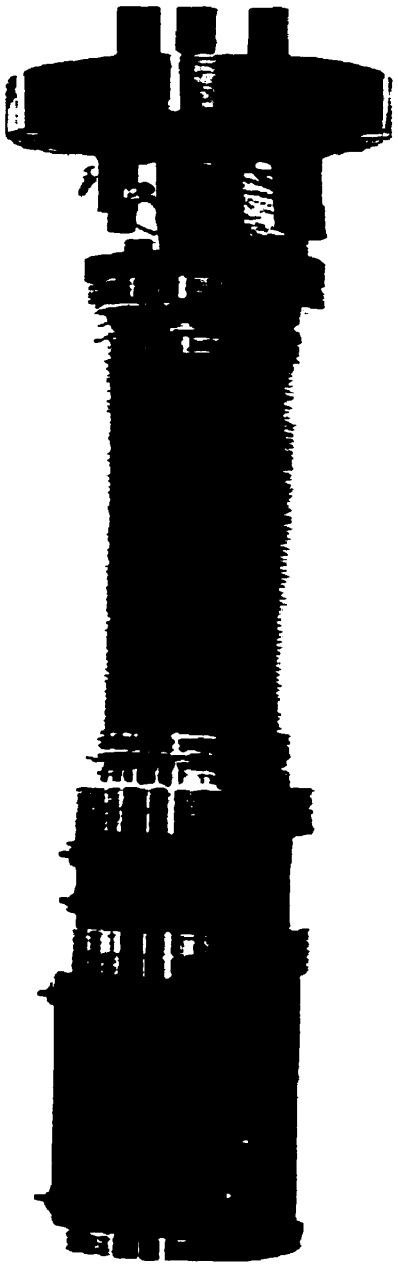


Figure 3.2: Photograph of the vacuum can contents, including the bellows and the linear positioners.

of the material is roughly equal to the adsorptivity, and that the radiating surface areas of the two reservoirs are approximately equal, the net heat transport between the two reservoirs is then given by

$$\dot{Q} = \sigma(\epsilon_1 - \epsilon_2)A({T_h}^4 - {T_l}^4) \tag{3.2}$$

where $T_h$ and $T_l$ are the temperatures of the reservoirs ($T_h > T_l$), with corresponding emissivities $\epsilon_h$ and $\epsilon_l$.

In order to reduce heat transfer via radiation through the walls of the dewar, the vacuum space of our dewar is lined with low emissivity superinsulation. This material is a thin metallized insulator, usually aluminized mylar, about 0.00025" to 0.001" thick. To prevent adjacent layers from touching each other, the material is often corrugated. In a commercial superinsulated dewar, there are typically about 50 layers of superinsulation, corresponding to a thickness of about one inch [29]. The first few layers are the most effective in the attenuation of thermal radiation. The subsequent layers, however, are important for the suppression of thermal conductivity in any residual gas within the vacuum space of the dewar.

Located on the superconducting magnet support structure are a series of copper baffles. Annular in shape, they serve to block and attenuate radiation before it reaches the bottom of the dewar where the instrument resides. The final heat transferred to the experiment via thermal radiation is thereby reduced by a factor of $n + 1$, where $n$ is number of baffles used [29].

In order to monitor the level of liquid helium present in the dewar, a superconducting level detector is used. This device uses a piece of superconducting wire which has a transition point near 4.2 Kelvin. A current very near its critical current is driven through the wire, so that only the portion of the wire immersed in liquid helium remains superconducting, while the length above remains resistive. The resulting voltage along the sensor is proportional to the length of the wire above the liquid. Because the measurement process dissipates heat, level readings are usually taken on an intermittent basis, although the small amount of heat generated in the probe is

dissipated primarily in the helium gas rather than in the liquid.

Our liquid helium level sensor uses a small niobium-titanium wire as the detector element, and is unaffected by magnetic fields of up to 10 Tesla. The level meter has a length of 24", though it has a nominal one-half inch non-active portion at the top and bottom of the sensor. The sensor is controlled by an American Magnetic, Inc. Model 134 Liquid Helium Level Monitor. It allows either for continuous reading or intermittent sampling, with time intervals ranging from 0.0 to 600.0 minutes or hours. The liquid helium level is indicated in either inches, centimeters, or as a percentage of the length of the probe.

## *3.2 Superconducting Magnet*

Superconducting magnets are routinely used to produce extremely high magnetic fields without requiring large power supplies needed for non-superconducting magnets. This is the result of the superconductors' ability to support a very high current density with a vanishingly small resistance.

The typical geometry of a superconducting magnet is that of a solenoid, which provides for a uniform field over a substantial volume, with a minimum in total stored energy. Magnetic fields of up to 9 Tesla (90 kilogauss) are usually produced with magnets wound using conductors which are comprised of many fine filaments of a niobium-titanium (NbTi) alloy embedded in a copper matrix. For fields in excess of 9 Tesla, a more expensive and brittle multifilamentary niobium-tin ($Nb_3Sn$) conductor is used in combination with niobium-titanium. The use of twisted multifilamentary wire improves the stability of the magnet by preventing "flux jumping" which results in heat dissipation in the magnet and limits the rate at which it can be energized. The windings are bonded with a high thermal conductivity epoxy to give mechanical stability and thus prevent relative movement resulting from Lorentz forces between the field and the current.

One of the main advantages of the superconducting magnet is its ability to operate in a "persistent mode". This mode is energized through the use of a "persistent

switch", which is a small length of superconducting wire wrapped with a heater wire, fitted in parallel with the main windings. When heated, the superconducting wire reverts to a highly resistive state; current flows through the superconducting windings and the power supply, which may then increase or decrease the current flowing in the magnet. When the heater is turned off, the persistent switch becomes superconducting. The magnet and switch then form a completely closed superconducting circuit, through which the current circulates. The power supply can then be disconnected from the magnet. While in persistent mode, the magnetic field decays according to

$$H = H_0 e^{-t/\tau} \tag{3.3}$$

where $H$ is the field magnitude after a time $t$, $H_0$ is the initial field, and $\tau$ is the time constant of the magnet. The small residual resistance in the magnet occurs either from resistance in the joints between the sections of wire used to make the magnet, or from flux flow effects. A decay rate of 1 part in $10^4$ per hour is easily achieved in a typical magnet [30].

The homogeneity of the magnetic field is often specified over a 10 mm diameter spherical volume (d.s.v.). It is easy to achieve a homogeneity of 1 in $10^3$ in a solenoid type magnet. High resolution nuclear magnetic resonance and similar experiments are usually carried out in magnets with a homogeneity of 1 in $10^7$ or better over a 10 mm d.s.v. Increases in homogeneity typically require the use of additional "compensation coils" that can be used to fine-tune the field profile by reducing finite winding length effects. Figure 3.3 shows a graph of the theoretical axial magnetic field of our magnet as a function of axial position. The field decreases approximately quadratically with axial distance from the centre.

Our system uses an 80 kilogauss niobium-titanium superconducting magnet from American Magnetics, Inc. It is controlled using an AMI Model 412 Magnet Power Supply Programmer, which incorporates a power supply programmer, a magnet voltage indicator, and a regulated current source for the magnet persistent switch heater. A magnet quench protection circuit is also incorporated into the unit, which in the

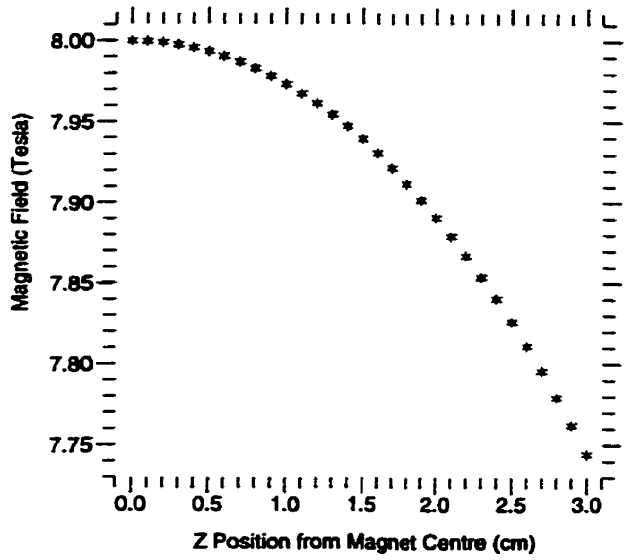


Figure 3.3: Graph of the theoretical axial magnetic field as a function of axial position, for our superconducting magnet. Courtesy of American Magnetics, Inc.

event of a quench, quickly ramps the power supply output to zero. The programmer can be operated either manually or via computer. The power supply is an American Magnetics 1 kW, EMSII model 10-100. It uses a reverse biased heat sunk diode, rated for continuous operation at the full output current of the supply, in order to prevent a high voltage from being generated across the input terminals of the magnet in the event of a quench.

## 3.3 *Cryostat*

The cryostat, which is inserted into the dewar, is comprised of a vacuum can suspended by three thin-walled tubes. The vacuum can, made of 0.028" thick stainless steel, has a nominal diameter of 2.5", and is sealed using an indium o-ring secured with eight bolts. It was designed specifically so as to allow the can to be placed within the 3" bore of the superconducting magnet. The three supporting tubes are made of 3/8" outer diameter, 0.020" thick stainless steel. The poor thermal conductivity and small wall thickness of these tubes help to minimize the heat conduction down into the dewar. All the microscope control cables and fibre optics are resident in two of

| Magnet Characteristic | Value |
|---|---|
| Rated Central Field @ 4.2 K | 8.0 Tesla |
| Rated Current | 83.2 Amps |
| Maximum Test Field @ 4.2 K | 8.2 Tesla |
| Field to Current Ratio | 0.0962 Tesla/Amp |
| Homogeneity over 1 cm DSV | ± 0.1 % |
| Measured Inductance | 11.7 Henries |
| Suggested Charging Voltage | 1.3 Volts |
| Clear Bore | 3.0 inches |
| Overall Length (flange to flange) | 8.3 inches |
| Maximum Outside Diameter | 5.75 inches |
| Weight | 25 lbs. |
| Recommended Persistent Switch Heater Current | 42 mA |
| Room Temperature Persistent Switch Heater Nominal Resistance | 76 Ω |
| Room Temperature Magnet Resistance in Parallel with Switch | 14 Ω |

Table 3.1: Specifications of our superconducting magnet, courtesy of American Magnetics, Inc.

these tubes. The third tube is used exclusively as a pumping line, which is connected to our Balzers TCP 121 turbomolecular pump using kwik flanges and viton o-rings.

A series of baffles are attached to the three tubes, at heights equivalent to those of the baffles located on the magnet support structure. Circular in shape, these copper baffles compliment the centre hole of the annular baffles. In addition to attenuating radiation, they also force the helium gas to flow in a turbulent fashion as it exits the dewar. This allows the relatively large enthalpy of the gas to contribute to the cooling process. Several holes were drilled in each baffle to allow for the unimpeded rapid escape of large amounts of helium vapour in the event of a superconducting magnet quench.

## 3.4 Thermometer

To measure the temperature of our system, we use a CD-301 Silicon Diode Cryogenic Temperature Sensor from T·R·I Research. The diode is mounted in a bobbin configuration of gold plated copper, with polyimide insulated phosphor-bronze 36 AWG lead wires. It covers a temperature range from 1.5 to 373 Kelvin, producing a voltage

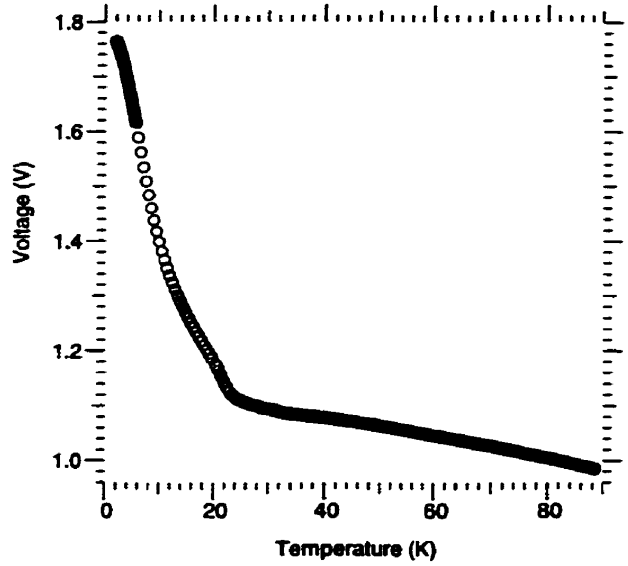


Figure 3.4: Calibration curve showing output voltage vs. temperature for our silicon diode thermometer.

between 0.4 and 2.0 volts which is monitored with a Keithley Model 2000 6.5 digit digital multimeter. The 10 $\mu$A excitation current is provided by a Lakeshore Model 120 current source. Reported sensitivities are 2.8 mV/K above 25 Kelvin and 40 mV/K below 25 Kelvin, with a thermal time constant of 10 msec at 4.2 Kelvin and a heat dissipation of 20 microwatts at 4.2 Kelvin. The thermometer does not conform to a standard calibration curve, but was calibrated for us by the Superconductor Group at McGill University, headed by Dr. Louis Taillefer. The calibration curve for this thermometer is shown in Figure 3.4.

## 3.5 *Low Temperature Considerations*

Quite separate from the design issues related to building an Atomic Force Microscope, it is important to appreciate that the system will be operating at low temperatures. Cryogenic instruments such as this require additional design and operating considerations, most of which deal with the problem of how to thermally isolate the microscope from its surroundings.

Listed in Table 3.2 are some characteristics of various cryogenic fluids. We use

| Gas | $O_2$ | $N_2$ | $^4He$ |
|---|---|---|---|
| Latent heat of vaporization (J/g) | 213 | 199 | 20.6 |
| Latent heat of vaporization (J/ml) | 243 | 161 | 2.6 |
| Enthalpy change of gas (J/g) 4.2 K - 77 K | — | — | 384 |
| Enthalpy change of gas (J/g) 77 K - 273 K | — | 234 | 1542 |
| Boiling point (K) | 90.2 | 77.3 | 4.2 |
| Liquid Density (g/ml) | 1.14 | 0.81 | 0.125 |

Table 3.2: Various characteristics at standard atmospheric pressure for cryogenic fluids. From [30] and [31].

liquid nitrogen to pre-cool the dewar, and liquid helium to keep the microscope cold during operation. One litre of liquid helium expands to 750 litres of gas at room temperature and atmospheric pressure. One litre of gas at 4.2 Kelvin expands to 70 litres at room temperature and atmospheric pressure. Liquid helium has a very low latent heat of vaporization: that is, only a very small amount of heat is required to boil it (a heat load of 1 Watt will boil 1.4 litres of liquid per hour). However, the helium gas has a very high enthalpy - in other words, it is very easy to generate gas at 4.2 Kelvin, but it is much more difficult to warm that gas up. Given that helium has such a low latent heat of vaporization, it is important that the experimental setup be efficiently isolated from the environment. If this is not done well, not only will it increase the day-to-day operating costs, through liquid helium boiloff, but it can also limit the attainable base temperature of the cryostat.

### *3.5.1 Special Materials*

Operating a cryogenic instrument requires the use of several specialized materials. Primarily these materials are chosen for their low heat transport properties and their ability to thermally cycle without incurring damage.

In terms of heat conduction, the amount of heat, $\dot{Q}$, flowing between two thermal reservoirs at temperatures $T_2$ and $T_1$ with $T_2 > T_1$, linked by a solid bar of material of uniform cross sectional area A, is given by Fourier's Law,

$$\dot{Q} = \kappa A \nabla T \tag{3.4}$$

| Material | $\bar{\kappa}$ $T_2 = 300$K $T_1 = 77$K | $\bar{\kappa}$ $T_2 = 300$K $T_1 = 4$K | $\bar{\kappa}$ $T_2 = 77$K $T_1 = 4$K |
|---|---|---|---|
| Nylon | 0.31 | 0.27 | 0.17 |
| Pyrex Glass | 0.82 | 0.68 | 0.25 |
| Stainless Steel | 12.3 | 10.3 | 4.5 |
| Constantan (60 Cu, 40 Ni) | 20 | 18 | 14 |
| Brass (70 Cu, 30 Zn) | 81 | 67 | 26 |
| Copper (phosphorus deoxidized) | 190 | 160 | 80 |

Table 3.3: Mean values of thermal conductivity for various materials expressed in units of W/m-K. From [31].

where $\kappa$ is the thermal conductivity of the material, and $\nabla T$ is the vector temperature gradient between the two reservoirs. Thus, if the ends of the bar of length $l$ are at temperatures $T_1$ and $T_2$,

$$\dot{Q} = \frac{A}{l}\int_{T_1}^{T_2} \kappa(T)dT \tag{3.5}$$

where $\kappa(T)$ is the temperature-dependent thermal conductivity of the metal. This variable has been calculated for several common materials and end temperatures arising most often in cryogenic work. Values of the mean heat conductivity, given by

$$\bar{\kappa} = \frac{1}{(T_2 - T_1)}\int_{T_1}^{T_2} \kappa T dT \tag{3.6}$$

are listed in Table 3.3.

The other important criteria for material selection is that of thermal contraction. Since materials shrink upon cooling, it is important that all components of the microscope have similar expansion coefficients. Of course, a symmetric design also helps to ensure that any contraction experienced by the components does not disturb the overall symmetry of the instrument. Listed in Table 3.4 are the thermal contractions of some commonly used materials.

## 3.6 Vibration Isolation

The AFM images surfaces via micromechanical detection. External vibrations, such as those resulting from the movement of the building, from people walking and talking,

| Material | Contraction (per $10^4$) |
|---|---|
| Teflon | 210 |
| Nylon | 139 |
| 304 Stainless Steel | 30 |
| Aluminum | 41.4 |
| Silicon | 2.16 |
| Titanium | 15.1 |
| Macor † | 16.7 |
| Torr Seal | 67.7 |
| Copper | 32.6 |

Table 3.4: Some thermal contractions of selected materials, measured as $(L_{293} - L_{4.2})/L_{293}$ between 293K and 4K, except †Macor, which is listed for temperatures between 300 K and 77 K. From [29], [31], [32], [33].

from pumps, etc., tend to cause unwanted motion of the tip with respect to the sample. In order that these external vibrations do not limit the performance of the instrument, care must be taken to ensure that it is properly mechanically isolated.

Though the AFM is a complicated three dimensional instrument, the problem of vibration isolation can be effectively treated using a one dimensional mass-spring system. In this example, the AFM is represented by a mass $M$ mounted on a frame, the displacement of which is described by the function $X(t)$. The displacement of the mass is given by $x(t)$. Our approach to vibration isolation is to mount the mass to the frame through the use of a soft bellows [34]. Mathematically, the bellows is equivalent to a spring, from which we derive

$$f = -k(x - X) \tag{3.7}$$

where $f$ is the restoring force of the spring acting on the mass, and $k$ is the stiffness of the spring. In addition, we may add a damping force acting between the mass and the frame, which is characterized by the damping constant $\gamma$. Solving the equation of motion for the mass, assuming a sinusoidally varying driving force of frequency $\omega$, one obtains [25]

$$\frac{x_0}{X_0} = \frac{{\omega_0}^2 + 2i\gamma\omega}{{\omega_0}^2 - \omega^2 + 2i\gamma\omega} \tag{3.8}$$

where $x_0$ and $X_0$ represent the amplitude of the functions $x(t)$ and $X(t)$ respectively, and $\omega_0 = 2\pi f_0 = \sqrt{k/M}$. The ratio of the amplitudes is the transfer function of the vibration isolation system, and is given by [25]

$$K(\omega) \equiv \left|\frac{x_0}{X_0}\right| \equiv \sqrt{\frac{{\omega_0}^2 + 4\gamma^2\omega^2}{({\omega_0}^2 - \omega^2)^2 + 4\gamma^2\omega^2}} \tag{3.9}$$

An efficient vibration isolation system means a small $K(\omega)$. To achieve this, one must ensure that the natural frequency $\omega_0$ is made as low as possible. In that case, if the damping is negligible and the driving frequency is high relative to the natural frequency, the transfer function is given by [25]

$$K(\omega) \approx \left(\frac{\omega_0}{\omega}\right)^2 = \left(\frac{f_0}{f}\right)^2 \tag{3.10}$$

Though a low resonant frequency isolation system is beneficial, the AFM itself should have a high resonant frequency. This is easily seen by interpreting the frame as the base plate and sample of the AFM, and the mass as the cantilever and tip assembly. The model then describes the influence of external vibrations on the tip-sample displacement. When the excitation frequency is much lower than the natural frequency of the microscope, $f \ll f_0$, Eq. 3.8 becomes [25]

$$\frac{x_0 - X_0}{X_0} \approx \frac{f^2}{{f_0}^2} \tag{3.11}$$

Hence, by choosing a rigid microscope design, the low-frequency vibration does not affect the relative motion inside the instrument. For example, if the lowest resonant frequency of the AFM is greater than 20 kHz, a typical 20 Hz building vibration of amplitude 1 micron results in a relative tip motion of less than 0.01 Å, a nearly harmless level. Since available cantilever beams are made with high resonant frequencies, the limiting factor is usually the rest of the AFM [19].

Given an AFM with natural frequency $f_{\text{afm}}$, coupled to a vibration isolation system of natural frequency $f_{\text{vis}}$, subjected to vibrations with intermediate frequencies $f$ such that $f_{\text{vis}} < f < f_{\text{afm}}$, then the overall transfer function for the system is [25]

$$K(f) = \left(\frac{f}{f_{\text{afm}}}\right)^2 \left(\frac{f_{\text{vis}}}{f}\right)^2 = \left(\frac{f_{\text{vis}}}{f_{\text{afm}}}\right)^2 \tag{3.12}$$

In our system, the microscope is suspended from a stainless steel nested type bellows, purchased from Palatine Precision Ltd., of Rochester, Kent, England. These bellows have 70 convolutions, with a free pitch of 1.00 mm per convolution, an inner diameter of 26.50 mm, and an outer diameter of 42.40 mm. The spring rate per convolution is given as 3.5 kg/mm. The spring constant $k$, for the bellows assembly is then given by

$$k = \frac{\text{spring rate per convolution}}{\text{number of convolutions}} \tag{3.13}$$

$$= \frac{3.5 \text{ kg/mm}}{70}$$

$$= 490 \text{ N/m} \tag{3.14}$$

The lowest vertical resonance frequency of the bellows is then given by

$$f_0 = \frac{1}{2\pi}\sqrt{\frac{k}{M}} = \frac{1}{2\pi}\sqrt{\frac{g}{\Delta l}} \tag{3.15}$$

where $M$ is the total mass of the instrument suspended from the bellows. The measured mass $M$ of the microscope is 788 g. The resonance frequency may also be expressed as a function of the earth's gravitational acceleration $g$, and the elongation of the bellows under the weight of the instrument, $\Delta l = 12.7$ mm.

Both ends of the bellows are terminated by welded stainless steel flanges. A small hole in the bottom flange allows us the option of introducing an exchange gas into the interior of the bellows.

The acceleration spectrum of the nested bellows, measured in air with the microscope components suspended beneath, is shown in Figure 3.5. These measurements were made using an HS-J, 7.5 Hz Geophone seismometer from Geo Space Corporation. One was situated on the top flange, the other situated between the bottom of the bellows and the top of the microscope. The resonance peak of the system, shown on the solid line in the figure, is located at 3.9 Hz. From Eq. 3.15, one calculates a resonance frequency of 3.9 Hz using the measured value of $M$ and the calcuated value

of $k$, in perfect agreement with the experimental value. Taking $g$ as 9.81 m/s$^2$, the frequency is 4.4 Hz using the measured value of $\Delta l$. Using the experimental value of 3.9 Hz as the resonance frequency, the corresponding spring constant for the system is 473 N/m.

For comparison, we also characterized a small, stainless steel edge-welded bellows with a listed spring constant of 876 N/m. Illustrated in Figure 3.6 is the acceleration spectrum of these bellows with the microscope suspended from the bottom. The peak on the solid line at 8.3 Hz corresponds to a measured spring constant of about 2143 N/m, quite different from its listed value. This bellows was much more inflexible than the nested bellows, though it still performed surprisingly well, damping most accelerations by more than an order of magnitude over a 200 Hz bandwidth.

The transfer functions of the two bellows, calculated by dividing the solid by the dotted curves in each of Figures 3.5 and 3.6, are illustrated in Figure 3.7, along with the acceleration spectrum of the building excitations measured at the location of our instrument. This plot illustrates that for frequencies up to 30 Hz, the nested bellows does a better job at damping building vibrations. From 30 Hz to 180 Hz, both bellows seem comparable in their performance, with the exception of several prominent peaks appearing at 40 Hz, 80 Hz, 120 Hz and 160 Hz along the nested bellows trace. These resonances are attributed to internal resonances of the bellows, which we plan to dampen by wrapping it in teflon tape. Weights hung along the lamellae of the bellows may also be used for this purpose. At frequencies above 180 Hz, the two transfer functions appear to diverge. The trace of the edge welded bellows begins to increase, while the nested bellows continues to decrease, providing more effective isolation at these higher frequencies.

## 3.7 Microscope

One of the principal restrictions on the microscope which arises because of its cryogenic nature is that of size. Given that the instrument must fit within the restricted volume of the vacuum can, the design must be economical in its usage of space.

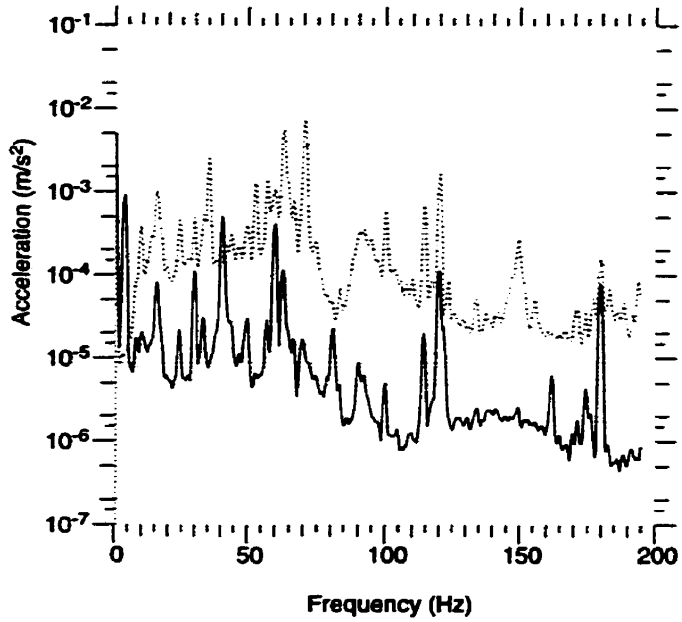


Figure 3.5: Acceleration spectrum of the nested bellows with the microscope suspended below, measured at the top flange (dotted line) and suspended from the bellows (solid line). Note the resonance peak at 3.9 Hz on the solid line.

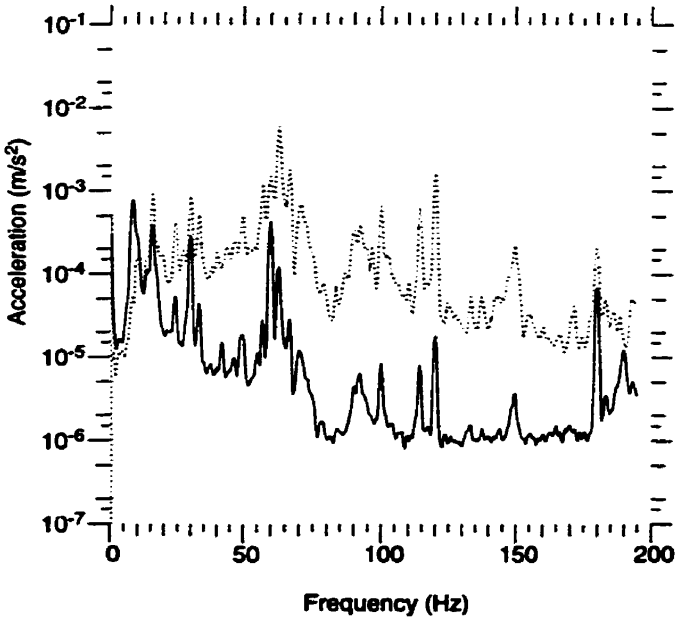


Figure 3.6: Acceleration spectrum of the edge-welded bellows with the microscope suspended below, measured at the top flange (dotted line) and beneath the bellows (solid line). The resonance peak for this system is at 8.3 Hz.

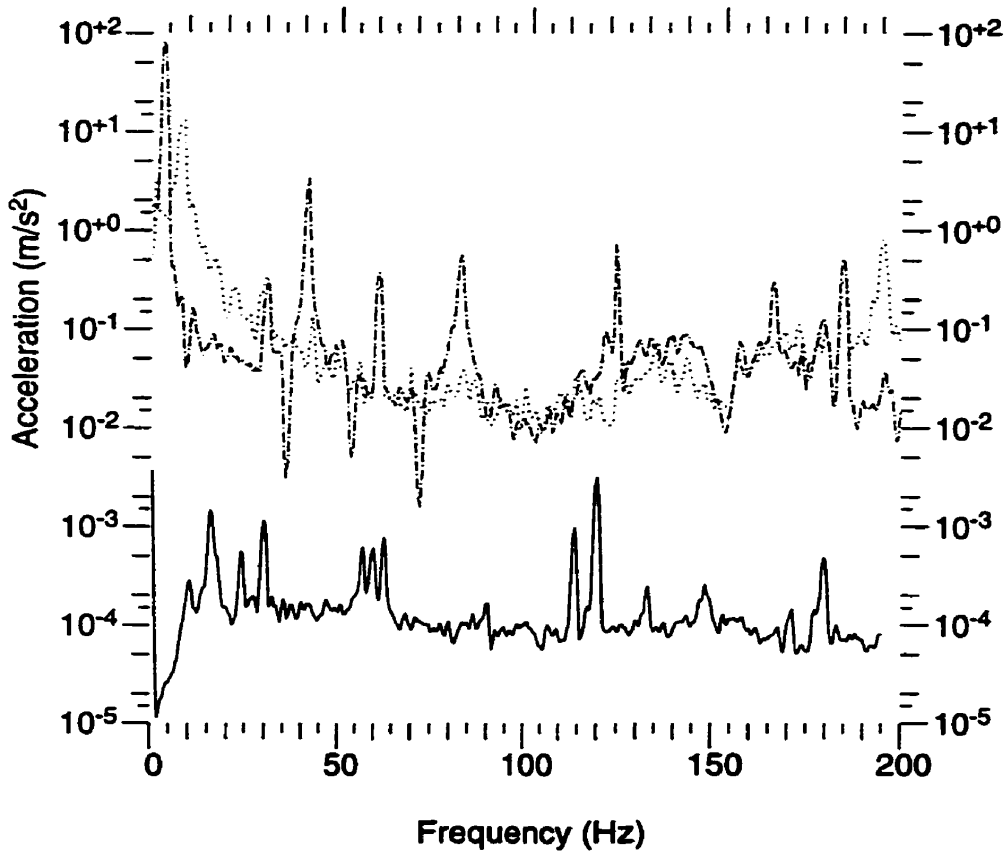


Figure 3.7: The transfer functions of the nested (dashdot line) and the edge-welded (dotted line) bellows, along with the acceleration spectrum of the building excitations (solid line). The axis on the left corresponds to the building vibrations, the axis on the right to the transfer functions. Note that the nested belllows provides better damping at frequencies below 30 Hz, which are typical of building vibrations. The peak at 120 Hz on the solid line is due to electromagnetic pickup of the coil used to measure the vibrations.

Another complicating issue is that of limited access, necessitating that any required adjustment of the components be performed remotely, without requiring the removal of the instrument from the vacuum can. The components of the microscope are discussed in the following sections.

### 3.7.1 *Fibre Optical Interferometer*

Our system uses an interferometer based on the all-fibre interferometer design described in [35] and [36]. Light from the laser diode is coupled into the single-mode optical fibre and propagates through a directional coupler, which acts like a beam splitter. Half of the light is directed to the end of the fibre near the cantilever, while the other half of the light may be coupled to a photodetector in order to monitor laser light intensity. This laser light reference monitor is not presently installed in our system. The cantilever end of the fibre is cleaved to permit a 4 % back-reflection of the incident light. This back-reflected light interferes with the light that exits the fibre and is reflected back into the fibre by the back side of the cantilever. For maximum sensitivity, the fibre end is positioned within a few microns of the back surface of the cantilever, maximizing the amount of reflected light coupled back into the fibre end. See Figure 3.8 for a schematic representation. The light intensity of the interference signal varies sinusoidally according to

$$I = \mid \vec{E}_R^2 + \vec{E}_{BR}^2 \mid = I_R + I_{BR} + \sqrt{I_R I_{BR}} \cos \Phi \tag{3.16}$$

where $\Phi$ is the phase difference between the electric fields of the reflected ($\vec{E}_R^2$) and back-reflected ($\vec{E}_{BR}^2$) beams, and $I_R$ and $I_{BR}$ the corresponding intensities. The phase difference depends on the optical path difference arising from the fibre-cantilever separation, and is given by

$$\Phi = \Phi_0 + \frac{4\pi\Delta z}{\lambda} \tag{3.17}$$

where $\Delta z$ is the fibre-cantilever separation, $\lambda$ is the wavelength of the laser light. For maximum sensitivity, the offset value $\Phi_0$ is typically set to $\Phi_0 = m\pi/2$, where $m$ is

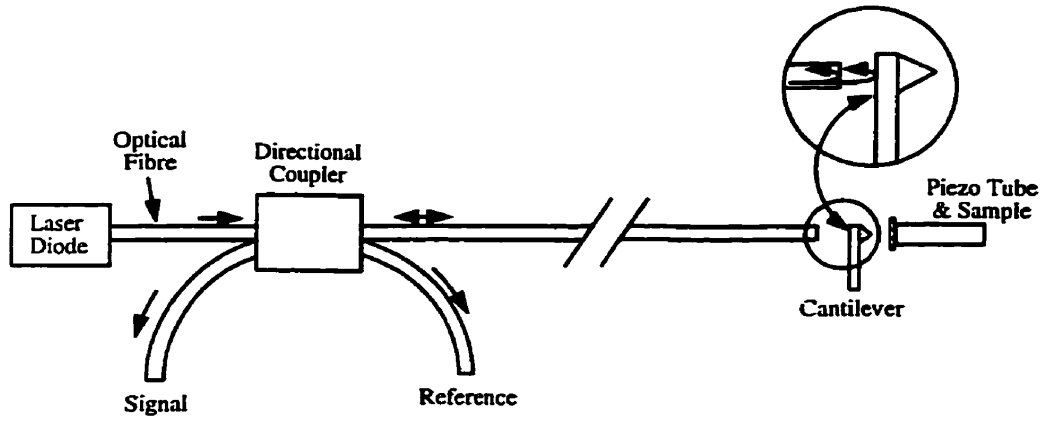


Figure 3.8: Illustration of the laser interferometer. The components on the left side are at room temperature. Those on the right are located within the vacuum can. Adapted from [1].

an integer, in order to shift the phase difference to the steepest portion of the cosine curve.

All of the electronic components of the interferometer are located outside of the cryostat and operate at room temperature. We use a Sharp LT023MSO FC connectorized single transmission-mode 780 nm semiconductor laser diode powered by an ILX Lightware LDX-3412 Precision Current Source. The laser light is coupled into a 3dB bidirectional coupler made by Gould Fiber Optics, which is in turn spliced to an 80 $\mu$m outer diameter, 4.5 $\mu$m core diameter 3M single mode fibre optic cable. A PIN-020A photodiode made by UDT Sensors Inc., measures the interference signal intensity.

### *3.7.2 Linear Positioners*

An important question regarding the design of the instrument is that of how to make in-situ mechanical adjustments. These include: (i) advancing the optical fibre towards the cantilever; (ii) approaching the piezo tube and sample assembly towards the cantilever; and (iii) laterally positioning the piezo tube and sample assembly with respect to the cantilever, so that various regions of the sample may be investigated. Adjustments of this nature are not easily made, and are further complicated by the fact that the microscope is operated both in vacuum and at low temperatures. Tradi-

tional mechanical feedthroughs are not practical from the perspective of the limited space available, as well as the low operating temperature of the instrument. Miniature electric motors are unsuitable, as they cannot be placed within the 8 Tesla magnetic field. Instead, our system uses a piezoelectric-based "clamping positioner".

The basic design of the positioner is illustrated in Figure 3.9. A central hexagonal prism is rigidly held within a surrounding outer shell. Six stacks of shear piezos (PZT-5A), each capped with aluminum oxide plates, are glued to three sides of the prism. The aluminum oxide plates contact the outer shell along sapphire strips, which function as wear surfaces. Spring tension washers are used to provide a loading force, which is evenly distributed using a point contact geometry provided by the sapphire ball bearing. This allows the positioner to be operated in either a vertical or horizontal manner. The piezo tube positioner is shown in Figure 3.10.

A schematic of the control circuit and principle of operation is shown in Figure 3.11. Power is supplied via the 110 Volt, 60 Hz ac line voltage, which is stepped up using a 2:1 transformer. A comparator is used to trigger on the maximum of the cycle. This voltage is then applied to the first piezo stack, causing it to bend. However, there is no relative movement between the hexagonal prism and the outer shell, since the five remaining stacks firmly clamp the prism in place. The voltage is then sequentially applied to the second and subsequent stacks, with a delay interval of 0.1 ms between stacks. Each time, the five static piezo stacks serve to prevent any motion of the hexagon while voltage is applied to the sixth stack. As the voltage waveform approaches zero, all six piezo stacks relax simultaneously, producing relative movement between the prism and the shell in the form of a "step". This process may be applied repeatedly at a frequency of 60 Hz in order to produce continuous motion. Movement in the opposite direction is accomplished by utilizing the negative portion of the voltage cycle.

A table-top prototype of this positioner was built out of aluminum in order to test the feasibility of the design and gain experience in its operation. An optical fibre was

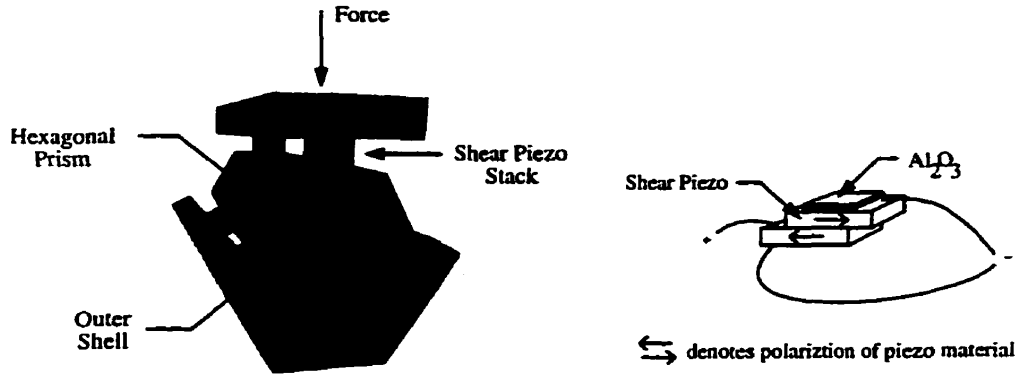


Figure 3.9: Illustration of the linear positioner used in our system. A hexagonal prism is held rigidly within a surrounding shell (left). Illustrated on the right is a detailed view of a shear piezo stack.

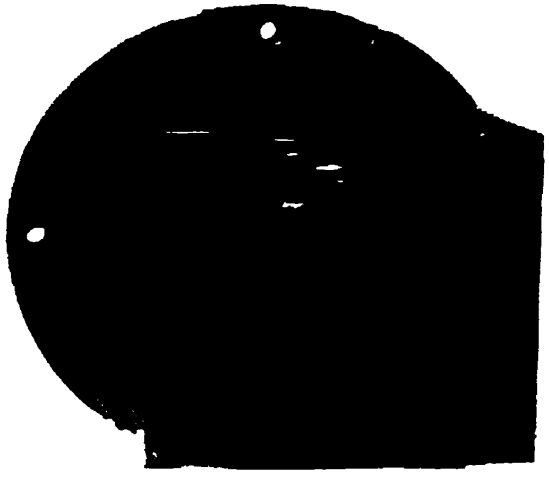

Figure 3.10: Front view of the piezo tube positioner used in the system. The front flange and top plate have been removed. Two piezo stacks are clearly visible on the top side of the hexagonal prism. The piezo tube, absent in this picture, normally sits within the hole of the hexagonal prism.

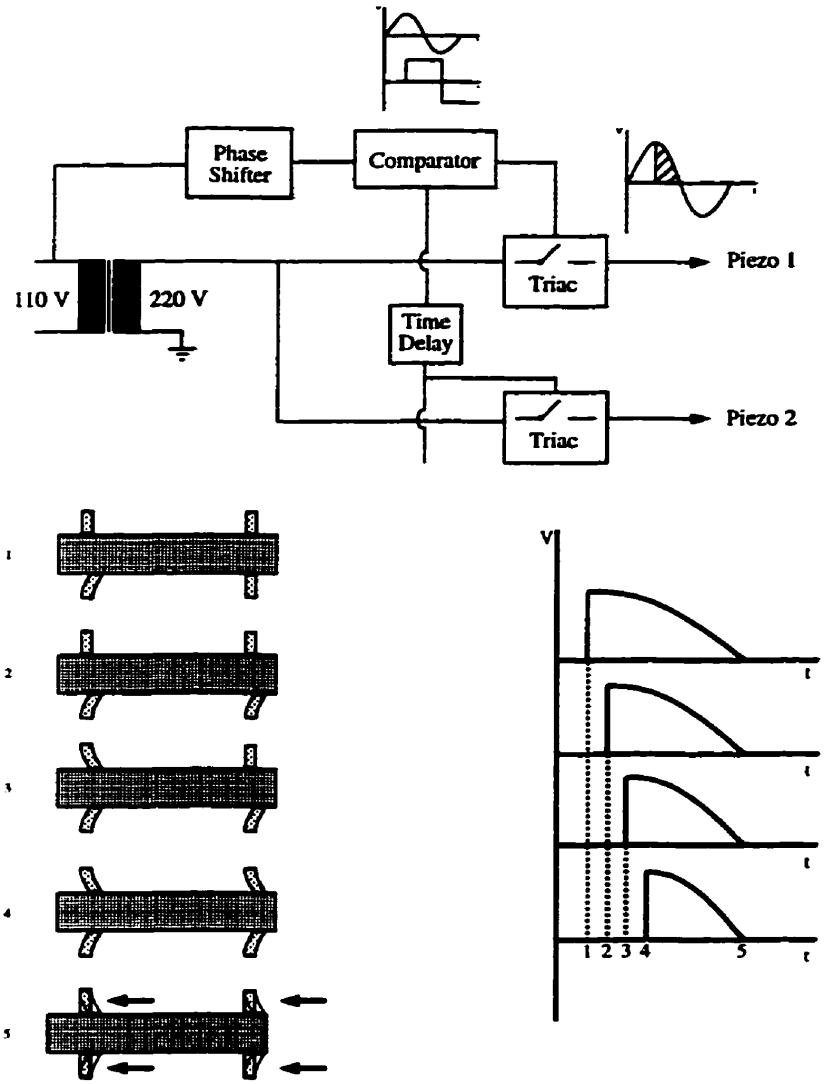


Figure 3.11: The principle of operation of the linear positioner. The top of the figure illustrates schematically the circuit used to control the positioner. The voltage waveforms of the six shear piezo stacks are shown below on the right side, with the corresponding motion of each of the piezo stacks illustrated on the left.

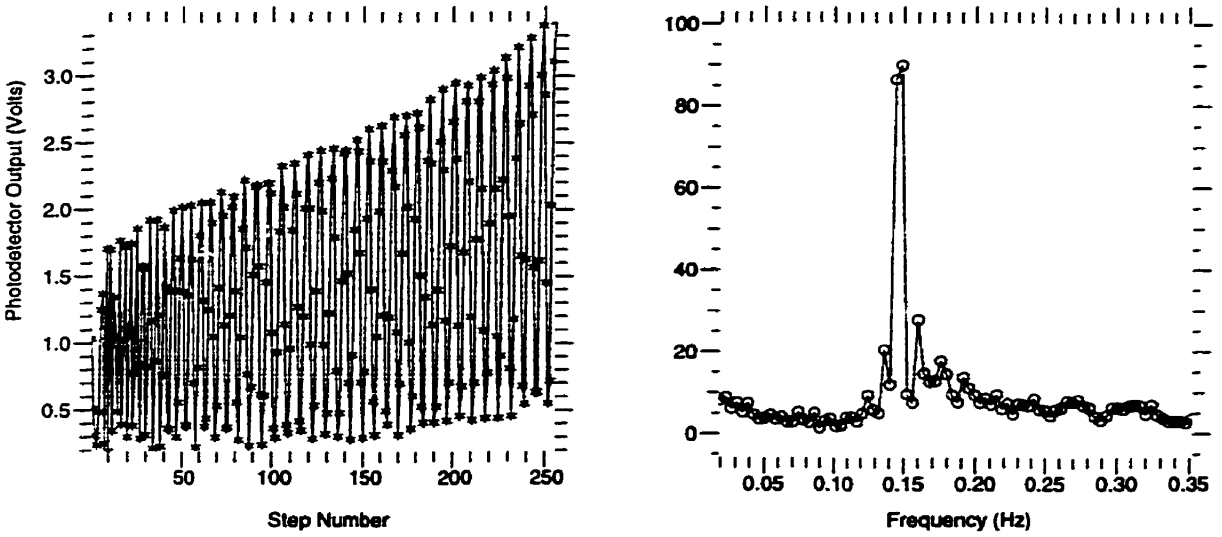


Figure 3.12: The optical interference signal from the linear positioner as it advances in air towards a silicon mirror (left), along with the corresponding Fourier transform (right).

mounted on the hexagonal prism in order to track its movement and measure the step size using interferometry. A computer was used to control the walker, advancing it by one step every second, while recording the resulting interference signal intensity. A sample of the photodetector output as the walker was approached in air to a silicon mirror is shown in Figure 3.12, along with the corresponding Fourier transform. Note that the amplitude of the interference signal increases as the fibre approaches the silicon mirror, since more reflected light couples back into the fibre. The transform shows a peak at about 0.1465 Hz, corresponding to an average step size of

$$\text{step size} = \frac{\text{walker movement}}{\text{number of steps}} \tag{3.18}$$

$$= 0.1465\,\frac{\lambda}{2}$$

$$\simeq 57 \text{ nm} \tag{3.19}$$

An average step size of 41 nm was found when the fibre was subsequently walked away from the silicon mirror. This variation in step size between forward and backward directions of travel was primarily attributed to the imperfections of the pro-

totype components. We also found the step size to be sensitive to a number of conditions, including the absolute position of the hexagonal prism with respect to its frame, the amount of pressure applied by the four springs, as well as the elapsed time after the start of motion. Clearly from Figure 3.12, the step size over the first fifty steps is larger than for the remaining steps.

A test of the prototype was also performed in liquid nitrogen with the optical fibre aligned with a cantilever, in order to determine whether lateral alignment is maintained during the cooling process. We found that in fact the fibre did stay aligned with the cantilever, and even managed to operate the walker while it was submerged within the liquid nitrogen. As a result, our system possesses no mechanism for lateral re-alignment of the fibre after the cooling process, but instead relies solely on the cylindrical symmetry of the microscope design.

Two linear positioners are used in our system, both constructed from stainless steel. One is used in order to approach the optical fibre towards the cantilever, while the other is used in order to approach the piezo tube and sample towards the cantilever (both of these adjustments are performed after the instrument has been equilibrated at 4.2 Kelvin). The optical fibre is glued into a fibre chuck, which is then secured in the hexagonal prism using two set screws. The piezo tube is glued to a piece of macor, which is in turn attached to its hexagonal prism using three screws.

### *3.7.3 Sample Scanner*

To scan our sample during the imaging process, we use a PZT-5H piezo tube purchased from Staveley Sensors, Inc. The tube is 2" long, with an outer diameter of 0.25", and a wall thickness of 0.05". We chose PZT-5H because of its high sensitivity, reflected in its relatively large $d_{31}$ coefficient, as compared with other commonly used PZT ceramics.

The theoretical scan range is given by Eq. 2.25. Using the value of $d_{31}$ for PZT-5H at 4.2 Kelvin, as listed in Table 2.2, and a nominal operating voltage of 400 Volts, we calculate a scan range of 4.2 $\mu$m.

### 3.7.4 *Electrical Connections*

For dc and low frequency signals, we used 0.005" diameter, Kapton coated twisted pair manganin wire to connect the top of the cryostat with the instrument at 4.2 Kelvin. Similar in its thermal and electrical properties to constantan, manganin is composed of 84% copper, 12% manganese, and 4% nickel. It was chosen because of its low thermal conductivity and its relatively constant resistivity with varying temperature[1]. With a room temperature resistivity of 48 $\mu\Omega$-cm [31], the measured resistance value from the top of the cryostat to the heat sink in the vacuum can was typically 60 $\Omega$. Twenty twisted pairs run though one 3/8" tube, 5 twisted pairs in another; each set terminates in a separate break-out box using BNC connectors. Within the vacuum can, 0.005" diameter Kapton coated copper wire and Samtec Micro Strip connectors were used.

For high frequency and especially sensitive measurements, coaxial cable was used. Made by Lake Shore Cryogenics, the Ultra Miniature Coaxial Cable is a 32 AWG stranded copper conductor with a Teflon insulator and a braided copper shield. The centre conductor is rated at 600 V DC max and 200 mA DC current, with a room temperature (293 Kelvin) resistance of 0.282 $\Omega$/m. Low temperature connections were made using Malco Lepra/Con Ultra Miniature coax connectors.

[1] Though it has a high electrical resistance, accurate resistance measurements can still be made using a four probe measurement technique.

# 4

# Outlook

Though nearly complete, at present the microsocpe is not yet operational. To achieve this goal, some additional work remains. In particular, the microscope requires: (i) the design and installation of an optimized cantilever holder; (ii) the installation of the piezo tube and fibre optic cable; (iii) additional wiring and heat sink work. One also anticipates that some time will be devoted towards debugging the instrument, once it is capable of producing images. The calibratioin grids we microfabricated at the University of Sherbrooke will be especially useful for this purpose.

Once the system is fully operational, a number of different experiments will be undertaken. In particular, we would like to investigate a number of phenomena that are either only observable at low temperature and/or that take advantage of the increased sensitivity of this instrument.

The planned projects can be divided into two categories. The first takes advantage of our low temperature capabilities, and is a straight foward extension of room temperature MFM, a technique with which our group has extensive experience. We will investigate the flux pinning mechanism in superconductors by imaging the flux lattice in real space in the presence of an external magnetic field. The nature of flux lattices (ordered, glassy, etc.) is presently debated, and real-time imaging while varying both temperature and external magnetic field will allow us to map the nature of the flux lattice phase diagram of several high-Tc as well as many standard superconductors.

A second project in this category involves the observation of domain structures in various materials. For example, we will examine the change in the domain structure

of various spin glasses as a function of composition and temperature, in collaboration with the Mössbauer group at McGill University, headed by Dr. Dominic Ryan. We would also like to investigate the process of magnetic reversal in very small ferromagnetic particles. Our existing room temperature force microscope has been used to investigate such characteristics as domain structure dynamics and magnetic dissipation of these systems. We hope to extend this knowledge by imaging increasingly smaller microfabricated ferromagnetic particles as a function of temperature and applied field. Of key interest is the switching behaviour (i.e. how do the particles rotate their magnetization in an external field) as a function of temperature and applied field. This behaviour of small particles is presently not well understood, but has important implications for the physical limit on the density of magnetic data storage media as well as methods of controlling magnetic coercivity, and thus losses.

Our long term goal is to use this device as the foundation for a new type of microscope, capable of looking more deeply into the internal structure of materials. Magnetic Resonance Force Microscopy (MRFM) is a combination of NMR and MFM, and has been shown to allow the detection of the magnetic moment of $10^8$ protons. We believe that by using tip technologies used for MFM and by operating at 4 Kelvin, we will be able to achieve single proton sensitivity. This would allow for the three dimensional atomic scale mapping of complex molecules or the obsevation of macrosopic quantum tunneling of the magnetization in small iron particles.

# BIBLIOGRAPHY


[1] P. LeBlanc, *Design and Characteristics of a General Purpose Atomic Force Microscope*, M.Sc. Thesis McGill University (1995)

[2] G. Binnig and H. Rohrer, *Helv. Phys. Acta.* **55**, 726 (1982)

[3] G. Binnig, C. F. Quate, and Ch. Gerber, *Phys. Rev. Lett.* **56**, 930 (1986)

[4] P. Grütter, H. J. Mamin and D. Rugar, *Magnetic Force Microscopy*, Springer Ser. Surface Sciences, Vol. 28 (Springer, Berlin, Heidelberg 1992)

[5] E. Betzig and J. K. Trautman, *Science*, **257**, 189 (1992)

[6] R. Erlandsson, G. M. McClelland, C. M. Mate and S. Chiang, *J. Va. Sci. Technol.* **A6**, 266 (1988)

[7] Y. Martin, C. C. Williams and H. K. Wickramasinghe, *J. Appl. Phys.* **61**, 4723 (1987)

[8] T. R. Albrecht, P. Grütter, D. Horne and D. Rugar, *J. Appl. Phys.* **69**, 668 (1991)

[9] Y. Martin and H. K. Wickramasinghe, *Appl. Phys. Lett.* **50**, 1455 (1987)

[10] A. Volodin and C. Van Haesendonck, Preprint, submitted STM'97

[11] A. Renou, *Sources De Dissipation Des Structures Microfabriques*, McGill University, June 1997

[12] E. Meyer and H. Heinzelmann, *Scanning Force Microscopy*, Springer Ser. Surface Sciences, Vol. 28 (Springer, Berlin, Heidelberg 1992)

[13] E. Meyer, *Atomic Force Microscopy*, University of Basel

[14] Rebecca Howland and Lisa Benatar, *A Practical Guide to Scanning Probe Microscopy,* Park Scientific, 1993-1996

[15] T. R. Albrecht, S. Akamine, T. E. Carver and C. F. Quate, *J. Va. Sci. Technol.* **A8**, 3386 (1990)

[16] G. Y. Chen, R. J. Warmack. T. Thundat, D.P. Allison and A. Huang, *Rev. Sci. Instrum.* **65**, 2532 (1994)

[17] U. Dürig, J. K. Gimzewski and D. W. Pohl, *Phys. Rev. Lett.* **57**, 2403 (1986)

[18] U. Dürig, O. Zuger and D. W. Pohl, *Phys. Rev. Lett.* **65**, 349 (1990)

[19] D. Rugar and P. Hansma, *Physics Today* **43**, 23 (Oct. 1990)

[20] G. Meyer and N. M. Amer, *Appl. Phys. Lett.* **53**, 1045 (1988)

[21] S. Alexander, L. Hellemans, O. Marti, J. Schneir, V. Ealings, P. K. Hansma, M. Longmire and J. Gurley, *J. Appl. Phys.* **65**, 164 (1989)

[22] C. Schönenberger and S. F. Alvarado, *Rev. Sci. Instr.* **60**, 3131 (1989)

[23] M. Tortonese, R. C. Barrett and C. F. Quate, *Appl. Phys. Lett.* **62**, 834 (1993)

[24] Neil W. Ashcroft and N. David Mermin, *Solid State Physics*, Saunders College Publishing, 1976

[25] C. Julian Chen, *Introduction to Scanning Tunneling Microscopy* Oxford University Press, 1993

[26] *Guide To Modern Piezoelectric Ceramics,* (Morgan Matroc Inc.)

[27] *EBL Piezoceramic Tubes For Ultraprecise Positioning Applications,* (Staveley Sensors Inc., 1994)

[28] J. Dewar, *Proc. R. Inst. Gt. Br.*, **14**, 1 (1893)

[29] Robert C. Richardson and Eric N. Smith, *Experimental Techniques in Condensed Matter Physics at Low Temperatures*, Addison-Wesley Publishing Company Inc, 1988

[30] N. H. Balshaw, *Elementary Practical Cryogenics,* Oxford Instruments Ltd., 1990

[31] Guy K. White, *Experimental Techniques in Low-Temperature Physics, Third Edition*, Oxford University Press, 1979

[32] M.J. Mackowski, K. E. West, D. A. Samsel, L. B. Holdeman and P. N. Peters, *Cryogenics* **16**, 45 (1976)

[33] *Macor - Machinable Glass Ceramic,* Corning

[34] O. Züger, H. P. Ott and U. Dürig, *Rev. Sci. Instr.* **63**, 5634 (1992)

[35] D. Rugar, H. J. Mamin and P. Güthner, *Appl. Phys. Lett.* **55**, 2588 (1989)

[36] T. R. Albrecht, P. Grütter, D. Rugar and D. P. E. Smith, *Ultramicroscopy* **42-44**, 1638 (1992)